

APPLIED PHYSICS

Bias-preserving gates with stabilized cat qubits

Shruti Puri^{1,2*}, Lucas St-Jean³, Jonathan A. Gross³, Alexander Grimm^{2,4}, Nicholas E. Frattini^{2,4}, Pavithran S. Iyer⁵, Anirudh Krishna³, Steven Touzard^{2,4}, Liang Jiang^{2,4,6}, Alexandre Blais^{3,7}, Steven T. Flammia^{2,8}, S. M. Girvin^{1,2}

The code capacity threshold for error correction using biased-noise qubits is known to be higher than with qubits without such structured noise. However, realistic circuit-level noise severely restricts these improvements. This is because gate operations, such as a controlled-NOT (CX) gate, which do not commute with the dominant error, unbiases the noise channel. Here, we overcome the challenge of implementing a bias-preserving CX gate using biased-noise stabilized cat qubits in driven nonlinear oscillators. This continuous-variable gate relies on nontrivial phase space topology of the cat states. Furthermore, by following a scheme for concatenated error correction, we show that the availability of bias-preserving CX gates with moderately sized cats improves a rigorous lower bound on the fault-tolerant threshold by a factor of two and decreases the overhead in logical Clifford operations by a factor of five. Our results open a path toward high-threshold, low-overhead, fault-tolerant codes tailored to biased-noise cat qubits.

INTRODUCTION

With fault-tolerant quantum error correction (QEC), it is possible to perform arbitrarily long quantum computations provided that the error rate per physical gate or time step is below some constant threshold value and the correlations in the noise remain weak (1). Codes, such as the surface code, which involve only local operations, are attractive for practical realization. However, these codes come at the cost of demanding threshold requirements and prohibitively large overheads (2, 3). Current efforts in QEC are largely devoted to recovery from generic noise, which lacks any special structure. For example, in the widely studied depolarizing noise model, errors are represented with the stochastic action of the Pauli operators \hat{X} , \hat{Y} , and \hat{Z} , and the probability of these errors is assumed to be (roughly) equal. However, several types of physical qubits have a biased noise channel, that is, one type of error dominates over all the others. Some examples of such biased-noise qubits are superconducting fluxonium qubits (4), quantum-dot spin qubits (5, 6), nuclear spins in diamond (7), and many others. It is therefore natural to consider whether the threshold and overhead requirements for fault-tolerant QEC can be improved by exploiting the structure of the noise.

Some efforts have been made toward designing QEC codes for biased-noise qubits (8–13). In particular, recent studies have shown ultrahigh code capacity thresholds for surface codes tailored to biased noise (12, 13). The code capacity is calculated by assuming noisy data qubits and noiseless syndrome-extraction circuits. However, errors during gate operations or circuit-level noise must be taken into account to estimate the fault-tolerant threshold. In the case of qubits with biased noise, operations that do not commute with the dominant error can unbiases or depolarize the noise channel,

reducing or eliminating any advantages conferred by the original biased noise.

To illustrate this point, consider first a system that preserves the noise bias. Suppose that we have a gate

$$ZZ(\theta) = \exp(i\theta \hat{Z}_1 \hat{Z}_2 / 2) \quad (1)$$

between two qubits suffering only from phase-flip errors with a tunable phase angle θ . When $\theta = \pi/2$, we recover the usual controlled-phase gate, CZ, up to local Pauli rotations and an overall phase. The $ZZ(\theta)$ gate can be implemented with an interaction of the form $\hat{H}_{ZZ} = -V \hat{Z}_1 \hat{Z}_2$ with the evolution unitary $\hat{U}(t) = \exp(iVt \hat{Z}_1 \hat{Z}_2)$. A $ZZ(\theta)$ gate is realized at time $T = \theta/2V$. Suppose that a phase-flip error occurs in either of the two qubits at time $0 \leq \tau \leq T$, in which case the evolution is modified into $\hat{U}_e(T) = \hat{U}(T - \tau) \hat{Z}_{1/2} \hat{U}(\tau) = \hat{Z}_{1/2} \hat{U}(T)$. That is, an erroneous gate operation $\hat{U}_e(T)$ is equivalent to an error-free gate followed by a phase flip, and therefore, the $ZZ(\theta)$ gate preserves the error bias.

Now, consider a controlled-NOT (CX) gate between the two qubits, implemented with an interaction of the form

$$\hat{H}_{CX} = V \left[\left(\frac{\hat{I}_1 + \hat{Z}_1}{2} \right) \otimes \hat{I}_2 + \left(\frac{\hat{I}_1 - \hat{Z}_1}{2} \right) \otimes \hat{X}_2 \right]$$

with the evolution unitary $\hat{U}(t) = \exp(-i\hat{H}_{CX}t)$. Here, the qubits labeled 1 and 2 are the control and target, respectively. A CX gate is realized at time T when $VT = \pi/2$ and

$$\hat{U}(T) = \left[\left(\frac{\hat{I}_1 + \hat{Z}_1}{2} \right) \otimes \hat{I}_2 + \left(\frac{\hat{I}_1 - \hat{Z}_1}{2} \right) \otimes \hat{X}_2 \right]$$

where we have ignored an overall phase. In this case, a phase-flip error in the target qubit at time $0 \leq \tau \leq T$ modifies the evolution to

$$\begin{aligned} \hat{U}_e(T) &= \hat{U}(T - \tau) \hat{I}_1 \otimes \hat{Z}_2 \hat{U}(\tau) \\ &= \hat{I}_1 \otimes \hat{Z}_2 e^{iV(T-\tau)(\hat{I}_1 - \hat{Z}_1) \otimes \hat{X}_2} \hat{U}(T) \end{aligned} \quad (2)$$

Consequently, a phase-flip error is introduced in the control qubit depending on when the phase error on the target occurred. However, the phase flip of the target qubit during the gate propagates

¹Department of Physics, Yale University, New Haven, CT 06520, USA. ²Yale Quantum Institute, Yale University, New Haven, CT 06520, USA. ³Institut quantique and D'epartement de Physique, Universit'e de Sherbrooke, 2500 boulevard de l'Universit'e, Sherbrooke, Quebec J1K 2R1, Canada. ⁴Department of Applied Physics, Yale University, New Haven, CT 06511, USA. ⁵Institute of Quantum Computing, 200 University Of Waterloo, Waterloo, Ontario, Canada. ⁶Pritzker School of Molecular Engineering, University of Chicago, Chicago, IL 60637, USA. ⁷Canadian Institute for Advanced Research, Toronto, Ontario, Canada. ⁸Centre for Engineered Quantum Systems, School of Physics, University of Sydney, Sydney, NSW 2006, Australia.

*Corresponding author. Email: shruti.puri@yale.edu

as a combination of phase flip and bit flip in the same qubit (for $\tau \neq 0, T$). Application of the CX gate therefore reduces the bias of the noise channel by introducing bit flips in the target qubit. In the same way, coherent errors in the gate operation arising from any uncertainty in V and T will also give rise to bit-flip errors in the target qubit. As a result, a native bias-preserving CX gate seems to be unphysical (8, 14). This is a serious drawback because the CX is a standard gate required to extract error syndromes in many error-correcting codes, including codes tailored to biased noise (12, 13). In the absence of a bias-preserving CX, alternate circuits are required for syndrome extraction. This was achieved in (8), for example, using teleportation schemes that require several CZ gates, measurements, and state preparations. The added complexity, however, limits the potential gains in fault-tolerant thresholds for error correction with biased-noise qubits.

Here, we show that a radical solution to the problem of implementing a bias-preserving CX exists with two-component cat qubits realized in a parametrically driven nonlinear oscillator (15). We choose to work in a basis in which the cat states $|C_\alpha^\pm\rangle = \mathcal{N}_\pm(|\alpha\rangle \pm |-\alpha\rangle)$ define the X axis of the qubit Bloch sphere shown in Fig. 1A (that is, $|\pm\rangle \equiv |C_\alpha^\pm\rangle$). Here $|\pm\alpha\rangle$ are coherent states, which have the same amplitude but differ in phase by π , and $\mathcal{N}_\pm = 1/\sqrt{2(1 \pm e^{-2|\alpha|^2})}$ are the normalization constants. Note that the cat states are orthogonal, $\langle C_\alpha^- | C_\alpha^+ \rangle = 0$. For simplicity, we assume that the qubit is defined with real and positive α . The Z axis of the Bloch sphere, or the computational basis, is defined as,

$$|0\rangle = \frac{|C_\alpha^+\rangle + |C_\alpha^-\rangle}{\sqrt{2}}, |1\rangle = \frac{|C_\alpha^+\rangle - |C_\alpha^-\rangle}{\sqrt{2}} \quad (3)$$

Note that, in the limit of large α , the states $(|C_\alpha^+\rangle \pm |C_\alpha^-\rangle)/\sqrt{2}$ are exponentially close to the coherent states $|\pm\alpha\rangle$.

The cat states, or equivalently their superpositions, $|0\rangle$ and $|1\rangle$, are the degenerate eigenstates of a parametrically driven Kerr nonlinear oscillator (15). Compared to schemes based on harmonic oscillators (16–18), the advantage of the realization considered here is that the intrinsic Kerr nonlinearity, required to realize the cat qubit, also provides the ability to perform fast gates (19) [note that the Bloch sphere used in (19) is rotated from the one used here by 90° so that the Z and X axes are interchanged]. In addition, it has been theoretically shown that although phase flips increase linearly with the size of the cat α^2 , bit flips are exponentially suppressed (15, 20). As a result, this cat qubit exhibits a strongly biased noise channel. With these cats we show that it is possible to perform a native CX gate while preserving error bias. This gate is based on the topological phase that arises from the rotation of the cats in phase space generated by continuously changing the phase of the parametric drive. Because of the topological construction, the proposed CX gate preserves the error bias. Moreover, the noise channel of the gate also remains biased in the presence of coherent control errors. The ability to realize a bias-preserving CX gate differentiates the cat qubit from strictly two-level systems with biased noise and demonstrates the advantage of continuous-variable systems for fault-tolerant quantum computing.

This paper is organized as follows: We first describe the preparation of the driven cat qubit and present its error channel. We also discuss the implementation of trivially biased $Z(\theta)$ and $ZZ(\theta)$ gates. The $ZZ(\theta)$ gate can be used to reduce the overhead for magic-state distillation (10). We then show how the bias-preserving CX gate is implemented and provide the χ -matrix representation of the noisy gate. Lastly, to demonstrate the advantage of having physical bias-preserving CX gates, we analyze the scheme for concatenated error correction tailored to biased noise in (8). The scheme first uses a repetition code to correct for the dominant phase-flip errors. The overall noise strength after the first encoding is reduced compared

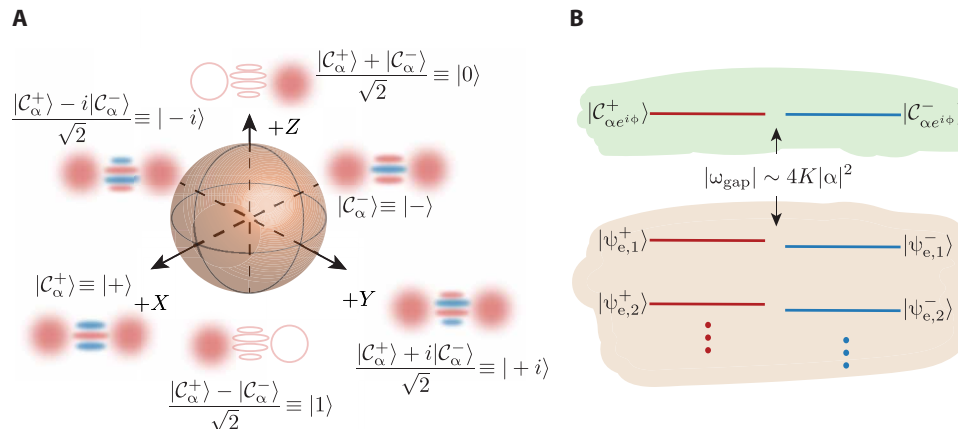


Fig. 1. Cat qubit in parametrically driven Kerr nonlinear oscillator. (A) Bloch sphere of the cat qubit. The figure also shows cartoons of the Wigner functions corresponding to the eigenstates of \hat{X} , \hat{Y} , and \hat{Z} Pauli operators. **(B)** Eigenspectrum of the two-photon, driven, nonlinear oscillator in the rotating frame. The Hamiltonian in the rotating wave approximation is given in Eq. 5. The cat states $|C_{\alpha e^{i\phi}}^\pm\rangle$ with $\alpha = \sqrt{P/K}$ are exactly degenerate. The eigenspectrum can be divided into an even- and odd-parity manifold. The cat subspace, highlighted in green, is separated from the first excited state by an energy gap $|\Delta\omega_{\text{gap}}| \sim 4K\alpha^2$. In the rotating frame, the excited states appear at a lower energy. This is because the Kerr nonlinearity is negative and implies that transitions out of the cat manifold occur at a lower frequency compared to transitions within the cat subspace. The energy difference between the first $n \sim \alpha^2/4$ pairs of excited states (highlighted in orange) $|\psi_{e,n}^\pm\rangle$ decreases exponentially with P or equivalently with α^2 . These excited state pairs are consequently referred to as quasi-degenerate states. In the limit of large α , the first n excited states are approximately given by $|\psi_{e,n}^+\rangle = (D(\alpha) \pm D(-\alpha))|n\rangle$ when n is even and $|\psi_{e,n}^+\rangle = (D(\alpha) \mp D(-\alpha))|n\rangle$ when n is odd (20). Here, $D(\pm\alpha) = \exp(\pm\alpha\hat{a}^\dagger \mp \alpha\hat{a})$ is the displacement operator, and $|n\rangle$ is the n -photon Fock state.

to the unencoded qubits, and the effective noise strength is more symmetric. The repetition code is then concatenated with a Calderbank, Shor, and Steane (CSS) code. We find that the availability of a bias-preserving CX considerably simplifies the gadgets needed to implement fault-tolerant logical gates. Consequently, we are able to achieve an increase in the threshold by a factor of $\gtrsim 2$ and a reduction in the overhead by a factor of $\gtrsim 5$ for the repetition code gadgets.

RESULTS

Two-photon driven nonlinear oscillator

The Hamiltonian of a two-photon driven Kerr nonlinear oscillator in a frame rotating at the oscillator frequency ω_r is given by

$$\hat{H}_0(\phi) = -K\hat{a}^{\dagger 2}\hat{a}^2 + P(\hat{a}^{\dagger 2}e^{2i\phi} + \hat{a}^2e^{-2i\phi}) \tag{4}$$

$$= -K(\hat{a}^{\dagger 2} - \alpha^2e^{-2i\phi})(\hat{a}^2 - \alpha^2e^{2i\phi}) + \frac{P^2}{K} \tag{5}$$

Here, K is the strength of the nonlinearity, while P and ϕ are the amplitude and phase of the drive, respectively, and $\alpha = \sqrt{P/K}$. The second line makes it clear that the even- and odd-parity cat states $|C_{\alpha e^{i\phi}}^{\pm}\rangle = \mathcal{N}_{\pm}(|\alpha e^{i\phi}\rangle \pm |-\alpha e^{i\phi}\rangle)$ are the degenerate eigenstates of this Hamiltonian (15, 21). Figure 1B shows the eigenstates of the oscillator in the rotating frame [see also (20) for a detailed discussion of the eigenspectrum].

Since Eq. 5 commutes with the photon number parity operator, its eigenspace can be divided into even- and odd-parity subspaces, labeled in the figure by the red and blue levels, respectively. The degenerate cat subspace \mathcal{C} (green) is separated from the rest of the Hilbert space \mathcal{C}_{\perp} (orange) by a large energy gap, which, in the rotating frame and in the limit of large α , is well approximated as $\Delta\omega_{\text{gap}} \sim -4K\alpha^2$. The negative energy gap implies that in the lab frame, transitions out of the cat manifold occur at a lower frequency compared to ω_r , the transition frequency within it. For large α , the energy gap between pairs of even- and odd-excited states $|\psi_{c,n}^{\pm}\rangle$ decreases exponentially for $n \lesssim \alpha^2/4$. As a result, the eigenspace of the two-photon driven oscillator reduces to $\alpha^2/4$ pairs of quasi-degenerate states (recall that the cat subspace is exactly degenerate). This Hilbert space symmetry is important for the exponential suppression of bit-flip errors. Moreover, observe that in the limit $P \rightarrow 0$, the even- and odd-parity cat states continuously approach the vacuum and single-photon Fock states, respectively. Consequently, starting from an undriven oscillator in vacuum (or single-photon Fock state), it is possible to adiabatically prepare the state $|C_{\alpha e^{i\phi}}^+\rangle$ (or $|C_{\alpha e^{i\phi}}^-\rangle$) by increasing the amplitude of a resonant two-photon drive at a rate $\ll 1/|\Delta\omega_{\text{gap}}|$ (15).

The phase ϕ of the two-photon drive is a continuous parameter that specifies the orientation of the cat in phase space. We define the cat qubit with the phase $\phi = 0$ (see Fig. 1A), and for the discussion of the following two sections, we will fix this phase. As we will see in a few sections, this phase degree of freedom is, however, crucial for the implementation of the CX gate.

Dynamics in the qubit subspace

Suppose that a single-photon drive is applied to the oscillator at the resonance frequency ω_r . In the rotating frame, the resulting Hamiltonian is $\hat{H}_1 = \hat{H}_0 + J(\hat{a}e^{-i\theta} + \hat{a}^{\dagger}e^{i\theta})$. Since coherent states are eigenstates of \hat{a} , it is easy to see that $\hat{a}|C_{\alpha}^{\pm}\rangle = \alpha r^{\pm 1}|C_{\alpha}^{\pm}\rangle$, where

$$r = \mathcal{N}_+/\mathcal{N}_- = \frac{\sqrt{1 - e^{-2\alpha^2}}}{\sqrt{1 + e^{-2\alpha^2}}} \sim 1 - e^{-2\alpha^2} \tag{6}$$

and the last expression is taken in the limit of large α . Unlike for \hat{a} , coherent states are not eigenstates of \hat{a}^{\dagger} . The action of \hat{a}^{\dagger} on a state in the cat subspace causes transitions to the excited states $\hat{a}^{\dagger}|C_{\alpha}^{\pm}\rangle \sim \alpha|C_{\alpha}^{\pm}\rangle + |\psi_{c,1}^{\mp}\rangle$. Recall that the cat subspace is separated from the rest of the Hilbert space by an energy gap. The applied drive, however, is at frequency ω_r , and therefore, the probability of excitation to the states $|\psi_{c,1}^{\mp}\rangle$ is suppressed by $\sim (J/\Delta\omega_{\text{gap}})^2$. On the other hand, these excitations would be permitted if the external drive had a frequency close to $\omega_r + \Delta\omega_{\text{gap}} \sim \omega_r - 4K\alpha^2$ (see the Supplementary Materials). Since the on-resonance drive only causes transitions within the cat subspace, the Hamiltonian projected onto \mathcal{C} is

$$\hat{P}_C\hat{H}_1\hat{P}_C = \alpha\cos(\theta)J(r+r^{-1})\hat{Z} + \alpha\sin(\theta)J(r-r^{-1})\hat{Y}$$

where $\hat{P}_C = |C_{\alpha}^+\rangle\langle C_{\alpha}^+| + |C_{\alpha}^-\rangle\langle C_{\alpha}^-|$ is the projection operator onto the cat subspace. In the limit of large α (or equivalently P), the above equation reduces to

$$\hat{P}_C\hat{H}_1\hat{P}_C \sim 2\alpha\cos(\theta)J\hat{Z} - 2\alpha\sin(\theta)Je^{-2\alpha^2}\hat{Y} \tag{7}$$

This expression shows that it is possible to implement an arbitrary rotation around the Z axis of the Bloch sphere using a single-photon drive by choosing $\theta = 0$ (15, 20). The angle of rotation is determined by the strength J , duration of the single-photon drive, and the amplitude α of the cat state. Equation 7 also shows that, unlike rotation around the Z axis, rotation around the Y axis is suppressed exponentially with α^2 . That is, the external drive couples predominantly to \hat{Z} . This observation implies that control errors (such as errors in the amplitude, frequency, phase, and duration of the single-photon drive) will lead to overrotation or underrotation around the Z axis but only cause exponentially small-angle rotations around the Y axis. Recall that for virtual excitations out of the cat subspace to be small, we require $J \ll |\Delta\omega_{\text{gap}}|$. That is, the energy gap governs rate of gate operations. It is easy to achieve $|\Delta\omega_{\text{gap}}|/2\pi \sim 200$ MHz in superconducting cavities, and therefore, fast rotations of $\lesssim 100$ ns are possible (19). This is to be contrasted with cat states produced in a harmonic oscillator by means of two-photon drive and dissipation (14, 22, 23). The ‘‘dissipative gap’’ that defines the cat qubit subspace is substantially smaller ($\lesssim 1$ MHz) (17, 18), and therefore, the gates are slower ($\gtrsim 1$ μ s.)

It is easy to extend the analysis above to realize a $ZZ(\theta) = \exp(i\theta\hat{Z}_1\hat{Z}_2/2)$ gate. This gate is implemented between two driven nonlinear oscillators coupled via a resonant beam splitter-type interaction (15, 24), $\hat{H}_{ZZ} = \hat{H}_{0,1} + \hat{H}_{0,2} + J_{12}(\hat{a}_1^{\dagger}\hat{a}_2 + \hat{a}_2^{\dagger}\hat{a}_1)$, with $\hat{H}_{0,i} = -K\hat{a}_i^{\dagger 2}\hat{a}_i^2 + P(\hat{a}_i^{\dagger 2} + \hat{a}_i^2)$, and $i = 1, 2$. For small J_{12} , the evolution under the Hamiltonian \hat{H}_{ZZ} is confined within the cat subspace and

$$\begin{aligned} \hat{P}_C\hat{H}_{ZZ}\hat{P}_C &= J_{12}\alpha^2(r^2+r^{-2})\hat{Z}_1\hat{Z}_2 + J_{12}\alpha^2(r^2-r^{-2})\hat{Y}_1\hat{Y}_2 \\ &\sim 2J_{12}\alpha^2\hat{Z}_1\hat{Z}_2 - 4J_{12}\alpha^2e^{-2\alpha^2}\hat{Y}_1\hat{Y}_2 \end{aligned} \tag{8}$$

The last line in the above equation is written in the limit of large α . In this limit, the term $\propto \hat{Y}_1\hat{Y}_2$ is negligibly small. Therefore, the unitary evolution under \hat{H}_{ZZ} realizes a $ZZ(\theta)$ gate with $\theta = 4J_{12}\alpha^2t_{\text{gate}}$,

where t_{gate} is the duration for which the beam-splitter coupling is turned on. Following the previous arguments, the control errors during this gate only lead to over- or underrotation around the Z axis, or correlated $\hat{Z}_1\hat{Z}_2$ errors. On the other hand, errors involving \hat{X}_i or \hat{Y}_i are exponentially suppressed with α^2 . We will now discuss the error channel of the cat qubit in more details and show that irrespective of the nature of the coupling with the bath, its error channel is biased toward dephasing errors.

Noise with narrow-band spectral density

Suppose that the oscillator couples to the environment with a general operator

$$\hat{O} = \sum_{m,n} \chi_{m,n}(t) \hat{a}^{\dagger m} \hat{a}^n + \text{h.c.} \tag{9}$$

From the analysis in the previous section, we see that $\hat{a}^{\dagger m}$ will cause excitations out of the cat subspace. In the limit of large α , $\hat{a}^{\dagger m}$ will excite the m th excited manifold. However, when the frequency spectrum of $\chi_{m,n}(t)$ is narrow and centered around $(n - m)\omega_r$, and $\max[|\chi_{m,n}(t)|] \alpha^{m+n-1} \ll |\Delta\omega_{\text{gap}}|$, then resonant (or real) and non-resonant (or virtual) excitations out of the cat manifold are negligible. The effect of the coupling in the cat manifold is then described by $\hat{P}_C \hat{O}_{m,n} \hat{P}_C = g_{m,n} f^{*m}(t) f^n(t) \hat{a}_C^{\dagger m} \hat{a}_C^n$. Here

$$\begin{aligned} \hat{a}_C &= \hat{P}_C \hat{a} \hat{P}_C = \alpha \left(\frac{r+r^{-1}}{2} \right) \hat{Z} + i\alpha \left(\frac{r-r^{-1}}{2} \right) \hat{Y} \\ \hat{a}_C^\dagger &= \hat{P}_C \hat{a}^\dagger \hat{P}_C = \alpha \left(\frac{r+r^{-1}}{2} \right) \hat{Z} - i\alpha \left(\frac{r-r^{-1}}{2} \right) \hat{Y} \end{aligned} \tag{10}$$

are the annihilation and creation operators projected onto the cat manifold. Note that for large α , we have $\hat{a}_C, \hat{a}_C^\dagger \approx \alpha \hat{Z} \mp i\alpha e^{-2\alpha^2} \hat{Y}$. Hence, we find that the oscillator-environment interaction is dominant along the Z axis ($\propto \alpha^{m+n}$), while suppressed along X and Y axes ($\propto \alpha^{m+n} e^{-2\alpha^2}$), and the resulting noise channel is biased. We now list the error channels for a few sources of narrow-bandwidth noise.

Thermal bath with narrow spectral density

By far, the main source of noise in oscillators is single-photon loss. In the cat subspace, one photon at a time is lost to the environment at frequency ω_r . However, it is also possible for the oscillator to gain photons if the bath is at nonzero temperature. If the spectral density of thermal photons is narrow, but smooth and centered around ω_r , then addition of a single photon to the oscillator (i.e., action of \hat{a}^\dagger) cannot cause transitions out of the cat subspace. The Born-Markov approximation in this limit leads to the Lindbladian $\mathcal{D}[\hat{O}_1]\hat{\rho} + \mathcal{D}[\hat{O}_2]\hat{\rho}$ (20) with

$$\begin{aligned} \hat{O}_1 &= \sqrt{\kappa[1 + n_{\text{th}}(\omega_r)]} \alpha \left[\left(\frac{r+r^{-1}}{2} \right) \hat{Z} + i \left(\frac{r-r^{-1}}{2} \right) \hat{Y} \right] \\ &\sim \sqrt{\kappa[1 + n_{\text{th}}(\omega_r)]} \alpha \left[\hat{Z} - i e^{-2\alpha^2} \hat{Y} \right] \end{aligned} \tag{11}$$

$$\begin{aligned} \hat{O}_2 &= \sqrt{\kappa n_{\text{th}}(\omega_r)} \alpha \left[\left(\frac{r+r^{-1}}{2} \right) \hat{Z} - i \left(\frac{r-r^{-1}}{2} \right) \hat{Y} \right] \\ &\sim \sqrt{\kappa n_{\text{th}}(\omega_r)} \alpha \left[\hat{Z} + i e^{-2\alpha^2} \hat{Y} \right] \end{aligned} \tag{12}$$

where the approximation is in the limit of large α . In the above expressions, $n_{\text{th}}(\omega_r)$ is the thermal photon number at ω_r . When $n_{\text{th}} = 0$, the above equation reduces to the master equation of the cat qubit coupled to zero temperature bath. Table 1 shows the error channel

corresponding to the above Lindbladian in the operator-sum representation, in the limit of small $\kappa\alpha^2 t$ for both $n_{\text{th}} = 0$ and $n_{\text{th}} \neq 0$.

Narrow spectral density frequency noise

Apart from gain and loss of photons, it is possible that coupling with the environment causes the frequency of the oscillator to fluctuate. This noise channel is often referred to as pure dephasing. However, if these fluctuations are slow and of small amplitude compared to the energy gap, such as in the case of flux noise in superconducting circuits (25, 26), then the out-of-cat excitations are suppressed. Consequently, in the Born-Markov approximation, the Lindbladian is given by $\mathcal{D}[\hat{O}]\hat{\rho}$ (20) with

$$\hat{O} = \sqrt{\kappa_\phi} \alpha^2 \left[\left(\frac{r^2 + r^{-2}}{2} \right) \hat{I} + \left(\frac{r^2 - r^{-2}}{2} \right) \hat{X} \right] \sim \sqrt{\kappa_\phi} \alpha^2 [\hat{I} - 2e^{-2\alpha^2} \hat{X}] \tag{13}$$

As before, the last term is an approximation in the limit of large α . Table 1 shows the corresponding error channel in the limit of small $\kappa_\phi \alpha^4 t$.

Noise with wide-band spectral density

The previous section described the noise channel of the cat qubit coupled to a bath with narrow-band spectral density so that leakage is avoided. However, what if the spectrum of the environment-oscillator coupling is such that leakage out of the cat subspace becomes non-negligible? First, we will show that the leakage errors can be autonomously corrected by addition of photon dissipation. Second, we find that the amount of nondephasing errors introduced because of the autonomous correction process depends on the energy difference between the even- and odd-parity states of the m th excited manifold $|\psi_{e,m}^\pm\rangle$. However, since this energy difference decreases exponentially with α^2 for $m < \alpha^2$, the nondephasing errors also remain exponentially suppressed with α^2 . It is important to emphasize that for the exponential suppression of nondephasing errors, the weight m must be smaller than the number of quasi-degenerate pairs of excited states $\alpha^2/4$. Therefore, it becomes possible to think of the driven nonlinear oscillator as a code that protects against nondephasing errors in the cat qubit. Moreover, the distance of this protection is $\sim \alpha^2/4$, which increases with the strength of the drive P . We explain these results further using explicit examples in the following sections.

Two-photon dissipation channel

In the presence of two-photon dissipation, the oscillator loses pairs of photons to the environment. The master equation of the parametrically driven oscillator in presence of a white two-photon dissipation channel is given by

$$\dot{\hat{\rho}} = -i[\hat{H}_0(\phi), \hat{\rho}] + \kappa_2 \mathcal{D}[\hat{a}^2]\hat{\rho} \tag{14}$$

where κ_2 is the rate of two-photon dissipation. Superconducting cavities with $\kappa_2/2\pi \sim 200$ kHz have been engineered (18). The dissipative dynamics can be understood in the quantum-jump approach in which the deterministic evolution governed by the non-Hermitian effective Hamiltonian $\hat{H} = \hat{H}_0(\phi) - i\kappa_2 \hat{a}^{\dagger 2} \hat{a}^2/2$ is interrupted by two-photon jump events. The non-Hermitian Hamiltonian is analogous to Eq. 5 with the Kerr nonlinearity K replaced by a complex quantity $K + i\kappa_2/2$. The nature of the eigenspectrum of the non-Hermitian

Downloaded from <http://advances.sciencemag.org/> on November 19, 2020

Table 1. Error channel of the cat qubit for different sources of decoherence. For the first three error sources, single-photon dissipation, thermal noise with narrow spectral density, and pure dephasing with narrow spectral density, it is possible to obtain an analytical expression for the channel. The expressions for the coefficients in the limit when the product of rate of decoherence and time is small (i.e., $\kappa\alpha^2 < 1$ and $\kappa_\phi t\alpha^4 < 1$) are given in the third column. Recall that $r = \sqrt{1 - e^{-2\alpha^2}}/\sqrt{1 + e^{-2\alpha^2}}$ approaches 1 in the limit of large α . Consequently, we find that all the coefficients involving the matrices \hat{X} and \hat{Y} are suppressed exponentially in α^2 .

Noise type	Error channel	Coefficients
Single-photon dissipation (bath at zero temperature)	$(\lambda_i\hat{I} + \lambda_x\hat{X})\hat{\rho}(\lambda_i\hat{I} + \lambda_x\hat{X}) + (\lambda_z\hat{Z} + i\lambda_y\hat{Y})\hat{\rho}(\lambda_z\hat{Z} - i\lambda_y\hat{Y})$	$\lambda_{i,X} = (\sqrt{1 - pr^{-2}} \pm \sqrt{1 - pr^2})/2$ $\lambda_{z,Y} = \sqrt{p}(r \pm r^{-1})/2, p = \kappa\alpha^2$
Thermal bath (narrow spectral density)	$(\lambda_i\hat{I} + \lambda_x\hat{X})\hat{\rho}(\lambda_i\hat{I} + \lambda_x\hat{X}) + (\lambda_z\hat{Z} + i\lambda_y\hat{Y})\hat{\rho}(\lambda_z\hat{Z} - i\lambda_y\hat{Y}) + (\lambda'_z\hat{Z} - i\lambda'_y\hat{Y})\hat{\rho}(\lambda'_z\hat{Z} + i\lambda'_y\hat{Y})$	$\lambda_{i,X} = (\sqrt{1 - p_1r^{-2}} - p_2r^2 \pm \sqrt{1 - p_1r^2 - p_2r^{-2}})/2$ $\lambda_{z,Y} = \sqrt{p_1}(r \pm r^{-1})/2, \lambda'_{z,Y} = \sqrt{p_2}(r \pm r^{-1})/2$ $p_1 = \kappa\alpha^2[1 + n_{th}(\omega_r)], p_2 = \kappa\alpha^2n_{th}(\omega_r)$
Pure dephasing (narrow spectral density)	$(\lambda_i\hat{I} + \lambda_x\hat{X})\hat{\rho}(\lambda_i\hat{I} + \lambda_x\hat{X}) + (\lambda_i\hat{I} - \lambda_x\hat{X})\hat{\rho}(\lambda_i\hat{I} - \lambda_x\hat{X})$	$\lambda_{i,X} = (\sqrt{1 - pr^{-4}} \pm \sqrt{1 - pr^4})/2$ $\lambda'_{i,X} = \sqrt{p}(r^2 \pm r^{-2})/2, p = \kappa_\phi t\alpha^4$
Thermal bath and two-photon dissipation (white spectral density)	$\lambda_{ii}\hat{\rho}\hat{I} + \lambda_{ix}\hat{I}\hat{\rho}\hat{X} + \lambda_{ix}^*\hat{X}\hat{\rho}\hat{I} + \lambda_{xx}\hat{X}\hat{\rho}\hat{X} + \lambda_{yy}\hat{Y}\hat{\rho}\hat{Y} + \lambda_{yz}\hat{Y}\hat{\rho}\hat{Z} + \lambda_{yz}^*\hat{Z}\hat{\rho}\hat{Y} + \lambda_{zz}\hat{Z}\hat{\rho}\hat{Z}$	See Eq. 18 and Fig. 2
Pure dephasing and two-photon dissipation (white spectral density)	$\lambda_{ii}\hat{\rho}\hat{I} + \lambda_{ix}\hat{I}\hat{\rho}\hat{X} + \lambda_{ix}^*\hat{X}\hat{\rho}\hat{I} + \lambda_{xx}\hat{X}\hat{\rho}\hat{X}$	See the Supplementary Materials.

Hamiltonian is therefore the same as the actual Hamiltonian of Eq. 5. However, unlike Eq. 5, the eigenenergies of \hat{H} become complex, implying linewidth broadening.

The cat states $|C_\beta^\pm\rangle$ are degenerate eigenstates of the non-Hermitian Hamiltonian $\hat{H}|C_\beta^\pm\rangle = E|C_\beta^\pm\rangle$, where E is a complex quantity $E = P^2/(K + i\kappa_2/2)$ and $\beta = e^{i\theta}\sqrt{P/(K + i\kappa_2/2)}$. Moreover, the cat states are also eigenstates of the two-photon jump operator $\hat{a}^2|C_\beta^\pm\rangle = \beta^2|C_\beta^\pm\rangle$. Therefore, the states $|C_\beta^\pm\rangle$ are invariant to two-photon dissipation. We have defined the cat qubit $|C_\alpha^\pm\rangle$ using real and positive coherent state amplitude α . For this qubit to be stabilized in the presence of two-photon dissipation, the phase and amplitude of the required two-photon drive are $2\phi_0 = \tan^{-1}(\kappa_2/2K)$ and $P = \alpha^2\sqrt{K^2 + \kappa_2^2}/4$, respectively.

Thermal bath with white-noise spectrum

White thermal noise leads to the Lindbladian master equation, $\dot{\hat{\rho}} = -i[\hat{H}_0(\phi), \hat{\rho}] + \kappa(n_{th} + 1)\mathcal{D}[\hat{a}]\hat{\rho} + \kappa n_{th}\mathcal{D}[\hat{a}^\dagger]\hat{\rho}$, where n_{th} is the number of thermal photons. Again, following the quantum-jump approach, the dynamics of the oscillator can be described by evolution under a non-Hermitian Hamiltonian $\hat{H} = \hat{H}_0(\phi) - i\kappa(1 + n_{th})\hat{a}^\dagger\hat{a}/2 - i\kappa n_{th}\hat{a}\hat{a}^\dagger/2$, which is interrupted by stochastic quantum jumps corresponding to the operators \hat{a}, \hat{a}^\dagger (27). When $\kappa \ll |\Delta\omega_{gap}|$, it is possible to replace \hat{a}, \hat{a}^\dagger with their projections in the cat basis $\hat{a}_C, \hat{a}_C^\dagger$ given in Eq. 10. As a result, the dominant effect of the non-Hermitian terms in \hat{H} is to broaden the linewidths of the cat states. A stochastic jump corresponding to the action of \hat{a} on a state in the cat-qubit subspace does not cause leakage. However, the action of \hat{a}^\dagger on a state in the cat subspace causes leakage, $\hat{a}^\dagger|C_\alpha^\pm\rangle \sim \alpha|C_\alpha^\mp\rangle + |\psi_{e,1}^\mp\rangle$ (note the change in parity). That is, $\langle\psi_{e,1}^\mp|\hat{a}^\dagger|C_\alpha^\pm\rangle \sim 1$ so that a

single-photon gain event excites the first excited subspace at a rate $\sim \kappa n_{th}$. This transition to the first excited state is illustrated in Fig. 2A. m photon gain events excite the m th excited subspace (with opposite parity if m is odd, or same parity if m is even). Suppose that a single-photon loss event followed a gain event. In this case, $\langle C_\alpha^\pm|\hat{a}|\psi_{e,1}^\pm\rangle \sim 1$, and hence, a single-photon loss event corrects the leakage at a rate $\kappa(n_{th} + 1)$. As a result, at steady state, the amount of leakage is $\sim \kappa n_{th}/\kappa(n_{th} + 1) \sim n_{th}$ (for $n_{th} \ll 1$). Now, suppose that a two-photon dissipation channel is introduced such that the rate of two-photon loss is κ_2 . In this case, $\langle C_\alpha^\pm|\hat{a}^2|\psi_{e,1}^\pm\rangle \sim 2\alpha$, and hence, a two-photon loss event will correct the leakage at a rate $4\kappa_2\alpha^2$. As a result, the residual leakage at steady state, is given by $\sim \kappa n_{th}/4\kappa_2\alpha^2 < n_{th}$ for $4\kappa_2\alpha^2 > \kappa$. Typically, in superconducting circuits $\kappa/2\pi \sim 10$ kHz, $n_{th} = 1\%$ so that even with a moderately sized cat $\alpha = 2$ and small amount of two-photon dissipation $\kappa_2/2\pi = 200$ kHz, the residual leakage is reduced to $\sim 3 \times 10^{-3}\%$.

Observe that the loss of two-photons causes transitions within the same parity subspace. Therefore, as illustrated in Fig. 2A, two-photon loss immediately after a single-photon gain event does result in phase flips. However, phase flips are already the dominant error channel in the system, and therefore, this effect does not change the structure of noise. However, the process of correcting leakage can also introduce bit flips. Before a two-photon jump event brings the population back to the cat manifold, the states $|\psi_{e,1}^\pm\rangle$ accumulate a phase proportional to their energies $E_{e,1}^\pm$, shown in the second panel in Fig. 2A. As a result, the population in the state $|\psi_{e,1}^\pm\rangle|C_\alpha^\pm\rangle$ and $|C_\alpha^\mp\rangle$ accumulates a phase difference $\propto (E_{e,1}^+ - E_{e,1}^-)$. In the cat qubit's computational basis $|0, 1\rangle = (|C_\alpha^\pm\rangle \pm |C_\alpha^\mp\rangle)/\sqrt{2}$, this corresponds to a bit flip. However, recall from Fig. 1B that $(E_{e,1}^+ - E_{e,1}^-)$ decreases

Downloaded from http://advances.sciencemag.org/ on November 19, 2020

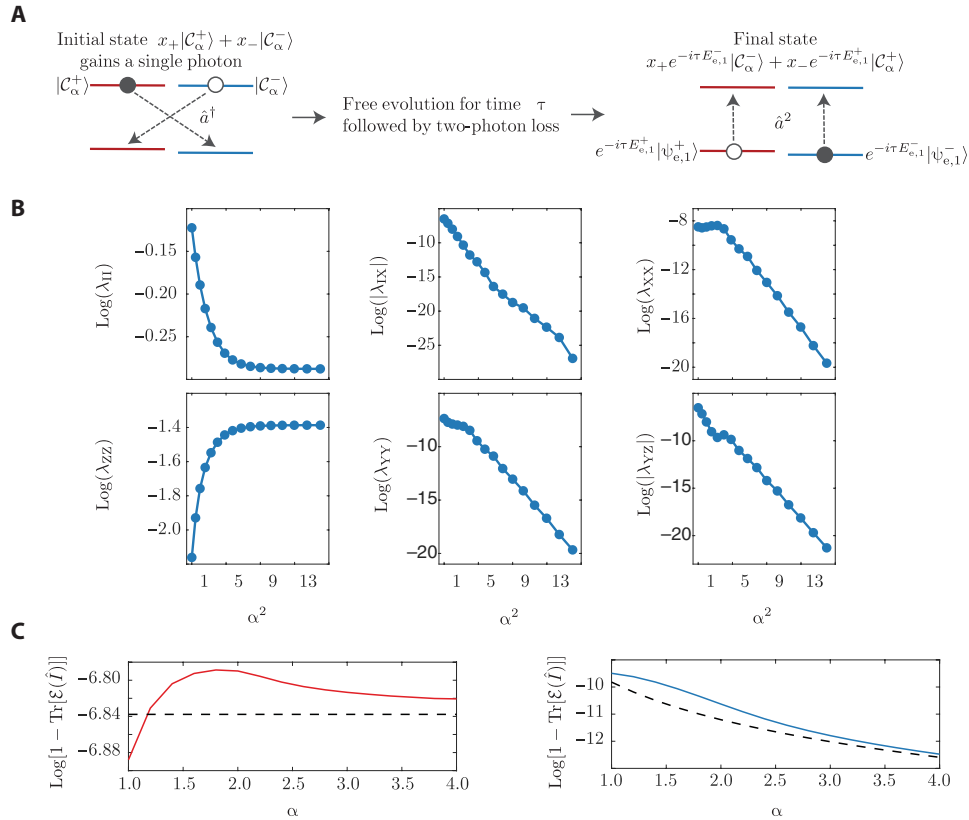


Fig. 2. Noise channel of the cat qubit in the presence of white thermal noise. (A) Addition of single photon at frequency $\omega_r + \Delta\omega_{\text{gap}}$ excites $|\psi_0\rangle = x_+|C_\alpha^+\rangle + x_-|C_\alpha^-\rangle$ to $x_+|\psi_{e,1}^-\rangle + x_-|\psi_{e,1}^+\rangle$. The state evolves freely for time τ , during which $|\psi_{e,1}^\pm\rangle$ acquire phases $\sim \tau E_{e,1}^\pm$. After loss of two photons, the final state is $x_+ e^{-i\tau E_{e,1}^-}|C_\alpha^-\rangle + x_- e^{-i\tau E_{e,1}^+}|C_\alpha^+\rangle \equiv \hat{Z} e^{i(\tilde{E}_{e,1}^- - \tilde{E}_{e,1}^+)x/2} |\psi_0\rangle$. Therefore, the autonomous correction of leakage leads to both dephasing and nondephasing error. However, $E_{e,1}^- - E_{e,1}^+$ decreases exponentially with α^2 , and hence, the nondephasing error is exponentially suppressed. **(B)** Natural logarithm of the coefficients of the error channel (Eq. 18) at $t = 50/K$ with $n_{\text{th}} = 0.01$, $\kappa = K/400$, and $\kappa_{2\text{ph}} = K/10$. As expected, the amount of non-phase errors decreases exponentially with α^2 . **(C)** Natural logarithm of the amount of leakage in the presence of white thermal noise without two-photon dissipation (red solid line in the left panel) and with it (blue solid line in the right panel). As expected, the two-photon dissipation autonomously corrects for leakage. The dashed black lines show the leakage predicted by the theoretical expressions for the rates of out-of-subspace excitations ($\sim \kappa n_{\text{th}}$) and correction due to single-photon loss $\sim \kappa(1 + n_{\text{th}})$ and two-photon loss $\sim 4\kappa_{2\text{ph}}\alpha^2$. These expressions are only approximations, which become more and more exact as α increases. The figure confirms that the numerically estimated leakage converges to the theoretically predicted value for large α .

exponentially with α^2 and the excited state manifold is quasi-degenerate. Consequently, the probability of a bit-flip error due to leakage also decreases exponentially with α^2 , and the noise bias is preserved.

To confirm the analysis above, we numerically evaluate the error channel of the cat qubit as a function of α^2 by simulating the master equation

$$\dot{\hat{\rho}} = -i[\hat{H}_0(\phi_0), \hat{\rho}] + \kappa(1 + n_{\text{th}})\mathcal{D}[\hat{a}]\hat{\rho} + \kappa n_{\text{th}}\mathcal{D}[\hat{a}^\dagger]\hat{\rho} + \kappa_{2\text{ph}}\mathcal{D}[\hat{a}^2]\hat{\rho} \quad (15)$$

The Hamiltonian $\hat{H}_0(\phi_0)$ stabilizes a cat qubit of real and positive amplitude α . This was discussed in the section titled “Two-photon dissipation channel”

$$\hat{H}_0(\phi_0) = -K\hat{a}^{\dagger 2}\hat{a}^2 + P(\hat{a}^{\dagger 2}e^{2i\phi_0} + \text{h.c.}) \quad (16)$$

$$2\phi_0 = \tan^{-1}(\kappa_{2\text{ph}}/2K), P = \alpha^2\sqrt{K^2 + \frac{\kappa_{2\text{ph}}^2}{4}} \quad (17)$$

From the simulations, we find that the error channel takes the form

$$\mathcal{E}(\hat{\rho}) = \lambda_{\text{II}}\hat{I}\hat{\rho}\hat{I} + \lambda_{\text{IX}}\hat{I}\hat{\rho}\hat{X} + \lambda_{\text{IX}}^*\hat{X}\hat{\rho}\hat{I} + \lambda_{\text{XX}}\hat{X}\hat{\rho}\hat{X} + \lambda_{\text{YY}}\hat{Y}\hat{\rho}\hat{Y} + \lambda_{\text{YZ}}\hat{Y}\hat{\rho}\hat{Z} + \lambda_{\text{YZ}}^*\hat{Z}\hat{\rho}\hat{Y} + \lambda_{\text{ZZ}}\hat{Z}\hat{\rho}\hat{Z} \quad (18)$$

The coefficients λ_{II} , λ_{IX} , etc. are shown in Fig. 2B at time $t = 50/K$ as a function of α for $n_{\text{th}} = 0.01$, $\kappa = K/400$, and $\kappa_{2\text{ph}} = K/10$. For a discussion on how the error channel is extracted from master equation simulations, see Methods. The time $50/K$ is chosen because it is the typical gate time on the stabilized cat qubit. As expected, for large $|\lambda_{\text{IX}}|$, $|\lambda_{\text{XX}}|$, $|\lambda_{\text{YZ}}|$, and $|\lambda_{\text{YY}}|$ decrease exponentially with α^2 . The amount of leakage is quantified by $1 - \text{Tr}[\mathcal{E}(\hat{I})]$, which is shown in Fig. 2C for $\kappa_{2\text{ph}} = 0$ (solid red line) and $\kappa_{2\text{ph}} = K/10$ (solid blue line). As expected, leakage decreases in the presence of two-photon dissipation. The simple theoretical model predicts that for large α , the leakage rate out of the cat manifold is $\sim \kappa n_{\text{th}}$. The rate at which the excited state population decays back to the cat manifold due to single- and two-photon dissipation is $\sim \kappa(1 + n_{\text{th}})$ and $\sim 4\kappa_{2\text{ph}}\alpha^2$,

respectively. Using these rates, it is possible to analytically estimate the amount of leakage, which is shown by the dashed black lines in Fig. 2C. The agreement between the numerical results and approximate analytical expressions is very good at large α .

Similar to thermal noise, frequency fluctuations of the oscillator can also have a white spectral density. In the Supplementary Materials, we discuss the error channel for white frequency noise and provide numerical estimate for the corresponding error channel. As expected, we find that the nondephasing errors are suppressed exponentially with α^2 .

The analysis in this section can easily be extended to any form of incoherent and coherent (or control) errors. We can now summarize the results for a general environment-oscillator interaction. Suppose that the system operator that enters in the interaction Hamiltonian is of the form $\sum_{m,n} \chi_{m,n} \hat{a}^{\dagger m} \hat{a}^n + \text{h.c.}$. The $\hat{a}^{\dagger m}$ term excites $|C_{\alpha}^{\pm}\rangle$ to the m th excited manifold $|\psi_{e,m}^{\pm}\rangle$. Addition of two-photon dissipation autonomously corrects for this leakage error. Moreover, if the order of \hat{a}^{\dagger} in the interaction is smaller than the number of pairs of quasi-degenerate excited states, $\alpha^2/4$, then the dominant error is of the form $f(\alpha) \hat{Z}$, while the nondephasing errors are exponentially suppressed. Here, $f(\alpha)$ is a polynomial function that depends on the details of the interaction and amount of two-photon dissipation added to correct for leakage. That is, the two-photon driven nonlinear oscillator effectively results in an inherent quantum code to correct for up to $\alpha^2/4$ bit-flip errors.

Bias-preserving CX gate

As discussed earlier, for the noise channel to remain biased, the time-dependent unitary describing the system evolution during the gate must not explicitly contain an \hat{X} operator. How can we then implement a CX gate? To build intuition on how to address this problem, it is useful to note that $\hat{X}|C_{\alpha}^{\pm}\rangle = \pm|C_{\alpha}^{\pm}\rangle$. Now, recall from Eq. 5 that the orientation of the cat state in phase space is defined by the phase ϕ of the two-photon drive. If this phase changes adiabatically from 0 to π , then the cat states $|C_{\alpha}^{\pm}\rangle$ transform to $|C_{\alpha}^{\pm}\rangle = \pm|C_{\alpha}^{\pm}\rangle$. Therefore, rotating the phase of the two-photon drive by π is equivalent to an \hat{X} operation. Our proposal for a two-qubit bias-preserving CX gate is based on this phase-space rotation of a target cat qubit conditioned on the state of a control cat qubit. In this section, we first describe the desired evolution of the system under a CX gate and show that this evolution preserves the bias. Subsequently, in the next section, we describe the underlying Hamiltonian achieving this evolution.

Consider two cat qubits each stabilized in a two-photon driven Kerr nonlinear oscillator. The initial state of the system is

$$|\psi(0)\rangle = (c_0|0\rangle + c_1|1\rangle) \otimes (d_0|0\rangle + d_1|1\rangle) \\ = (c_0|0\rangle + c_1|1\rangle) \otimes [(d_0 + d_1)|C_{\alpha}^+\rangle + (d_0 - d_1)|C_{\alpha}^-\rangle]$$

where the first and second terms in the tensor product refer to the control and target qubits, respectively. Now, suppose that the phase of the two-photon drive applied to the target oscillator is conditioned on the state of the control cat qubit so that at time t the state of the system is

$$|\psi(t)\rangle = c_0|0\rangle \otimes [(d_0 + d_1)|C_{\alpha}^+\rangle + (d_0 - d_1)|C_{\alpha}^-\rangle] + \\ c_1|1\rangle \otimes [(d_0 + d_1)|C_{\alpha e^{i\phi(t)}}^+\rangle + (d_0 - d_1)|C_{\alpha e^{i\phi(t)}}^-\rangle] \quad (19)$$

If the phase $\phi(t)$ is such that $\phi(0) = 0$ and $\phi(T) = \pi$, then at time T

$$|\psi(T)\rangle = c_0|0\rangle \otimes \{(d_0 + d_1)|C_{\alpha}^+\rangle + (d_0 - d_1)|C_{\alpha}^-\rangle\} + \\ c_1|1\rangle \otimes \{(d_0 + d_1)|C_{\alpha e^{i\pi}}^+\rangle + (d_0 - d_1)|C_{\alpha e^{i\pi}}^-\rangle\} \\ = c_0|0\rangle \otimes \{(d_0 + d_1)|C_{\alpha}^+\rangle + (d_0 - d_1)|C_{\alpha}^-\rangle\} + \\ c_1|1\rangle \otimes \{(d_0 + d_1)|C_{\alpha}^+\rangle - (d_0 - d_1)|C_{\alpha}^-\rangle\} \\ = c_0|0\rangle \otimes (d_0|0\rangle + d_1|1\rangle) + c_1|1\rangle \otimes (d_0|1\rangle + d_1|0\rangle) \\ = \hat{U}_{CX}|\psi(0)\rangle \quad (20)$$

As expected from the above discussion, a CX gate is realized by rotating the phase of the cat in the target oscillator by π conditioned on the control cat. The CX operation is based on the fact that during this rotation, the $|C_{\alpha}^-\rangle$ state acquires a π phase relative to $|C_{\alpha}^+\rangle$. This is a topological phase as it does not depend on energy like a dynamic phase or the geometry of the path like a geometric phase. This phase will arise as long as the states $|\pm\alpha\rangle$ move along a loop in phase space that does not come too close to the origin (see further discussion in the next section and the Supplementary Materials). If the number of times that the states $|\pm\alpha\rangle$ go around the origin to $|\mp\alpha\rangle$ is given by u , then the phase acquired by $|C_{\alpha}^-\rangle$ is $e^{iu\pi}$. That is, u is the winding number.

Coupling with the environment during this evolution leads to errors in both the control and target cats. From the analysis earlier in section titled “Noise with wide-band spectral density”, the predominant stochastic errors are of the form $\hat{O}_c = f(\alpha) \hat{Z}_c$ in the control cat and $\hat{O}_t^{\tau} = f'(\alpha e^{i\phi(\tau)}) \hat{Z}_t^{\tau}$ in the target cat where the superscript τ refers to the operator in the instantaneous basis of $\hat{Z}_t^{\tau} = |C_{\alpha e^{i\phi(\tau)}}^+\rangle \langle C_{\alpha e^{i\phi(\tau)}}^-| + |C_{\alpha e^{i\phi(\tau)}}^-\rangle \langle C_{\alpha e^{i\phi(\tau)}}^+|$. We now show that these dominant phase errors during the CX evolution propagate as phase errors. To see this, assume that a phase error occurred in the control qubit at time τ . Consequently, immediately after this error has occurred, the state of the system is

$$|\psi(\tau)\rangle_{\text{control}}^{\text{phase-flip}} = \hat{O}_c \otimes \hat{I}_t^{\tau} \{ c_0|0\rangle \otimes [(d_0 + d_1)|C_{\alpha}^+\rangle + (d_0 - d_1)|C_{\alpha}^-\rangle] + \\ c_1|1\rangle \otimes [(d_0 + d_1)|C_{\alpha e^{i\phi(\tau)}}^+\rangle + (d_0 - d_1)|C_{\alpha e^{i\phi(\tau)}}^-\rangle] \} \\ = c_0|0\rangle \otimes [(d_0 + d_1)|C_{\alpha}^+\rangle + (d_0 - d_1)|C_{\alpha}^-\rangle] - \\ c_1|1\rangle \otimes [(d_0 + d_1)|C_{\alpha e^{i\phi(\tau)}}^+\rangle + (d_0 - d_1)|C_{\alpha e^{i\phi(\tau)}}^-\rangle] \quad (21)$$

After this phase-flip event, the conditional phase continues to evolve and at time T

$$|\psi(T)\rangle_{\text{control}}^{\text{phase-flip}} = c_0|0\rangle \otimes [(d_0 + d_1)|C_{\alpha}^+\rangle + (d_0 - d_1)|C_{\alpha}^-\rangle] - \\ c_1|1\rangle \otimes [(d_0 + d_1)|C_{\alpha}^+\rangle - (d_0 - d_1)|C_{\alpha}^-\rangle] \\ = \hat{Z}_c \otimes \hat{I}_t^{\tau} \{ c_0|0\rangle \otimes [(d_0 + d_1)|C_{\alpha}^+\rangle + (d_0 - d_1)|C_{\alpha}^-\rangle] + \\ c_1|1\rangle \otimes [(d_0 + d_1)|C_{\alpha}^+\rangle - (d_0 - d_1)|C_{\alpha}^-\rangle] \} \\ = (\hat{Z}_c \otimes \hat{I}_t^{\tau}) \hat{U}_{CX}|\psi(0)\rangle \quad (22)$$

Therefore, a phase error on the control cat qubit at any time during the implementation of the CX is equivalent to a phase-flip

on the control qubit after an ideal CX. Now, assume that a phase error occurred on the target at time τ . Immediately after this error, the state is

$$\begin{aligned}
 |\Psi(\tau)\rangle_{\text{target}}^{\text{phase-flip}} &= \hat{I}_c \otimes \hat{O}_t^\tau \left\{ c_0 |0\rangle \otimes \left[(d_0 + d_1) |C_\alpha^+\rangle + (d_0 - d_1) |C_\alpha^-\rangle \right] + \right. \\
 &\quad \left. c_1 |1\rangle \otimes \left[(d_0 + d_1) |C_{\alpha e^{i\phi(\tau)}}^+\rangle + (d_0 - d_1) |C_{\alpha e^{i\phi(\tau)}}^-\rangle \right] \right\} \\
 &= f(\alpha) c_0 |0\rangle \otimes \left[(d_0 + d_1) |C_\alpha^+\rangle + (d_0 - d_1) |C_\alpha^-\rangle \right] + \\
 &\quad f(\alpha e^{i\phi(\tau)}) c_1 |1\rangle \otimes \left[(d_0 + d_1) |C_{\alpha e^{i\phi(\tau)}}^+\rangle + (d_0 - d_1) |C_{\alpha e^{i\phi(\tau)}}^-\rangle \right]
 \end{aligned} \tag{23}$$

As before, after this phase-flip event, the conditional phase continues to evolve, and at time T

$$\begin{aligned}
 |\Psi(T)\rangle_{\text{target}}^{\text{phase-flip}} &= f(\alpha) c_0 |0\rangle \otimes \left[(d_0 + d_1) |C_\alpha^+\rangle + (d_0 - d_1) |C_\alpha^-\rangle \right] + \\
 &\quad f(\alpha e^{i\phi(\tau)}) c_1 |1\rangle \otimes \left[- (d_0 + d_1) |C_\alpha^-\rangle + (d_0 - d_1) |C_\alpha^+\rangle \right] \\
 &= \hat{I}_c \otimes \hat{Z}_t \{ f(\alpha) c_0 |0\rangle \otimes [d_0 |0\rangle + d_1 |1\rangle] - f(\alpha e^{i\phi(\tau)}) c_1 |1\rangle \otimes [d_0 |1\rangle + d_1 |0\rangle] \} \\
 &= \left[\hat{Z}_c f(\alpha e^{i\phi(\tau)(1-\hat{Z}_c)}) \otimes \hat{Z}_t \right] \hat{U}_{\text{CX}} |\Psi(0)\rangle
 \end{aligned} \tag{24}$$

The above equations show that a phase-flip error on the target qubit at any time during the CX evolution is equivalent to phase errors on the control and target qubits after the ideal CX gate. That is, this CX gate based on rotation of the target cat qubit in phase space does not unbiased the noise channel. This is in stark contrast with the CX gate implementation between two strictly two-level qubits and shows the advantage of using the larger Hilbert space of an oscillator. Although we have only explicitly showed the bias-preserving nature of the CX with respect to one phase flip in either the control or target cats, it is easy to extend the analysis above to multiple phase flips to see that the bias remains preserved. Moreover, note that any control errors in the target or control qubit can be expanded in the form $\sum_{m,n,p,q} \chi_{m,n,p,q} \hat{a}_c^{\dagger m} \hat{a}_c^n \hat{a}_t^{\dagger p} \hat{a}_t^q$, where \hat{a}_c and \hat{a}_t are the annihilation operators for control and target oscillators, respectively. Of course, the terms $\hat{a}_c^{\dagger m}$, $\hat{a}_t^{\dagger p}$ will excite the control and target oscillators out of the cat qubit subspace. As we have already seen, addition of photon dissipation will autonomously correct this leakage while keeping bit flips exponentially suppressed as long as the weights $p, m < \alpha^2/4$. Small amounts of control error will only lead to low weight terms in the expansion above, and therefore, the bias will be maintained. We will now explain this more in detail with an example.

Suppose that the control error was such that at the end of the gate, $\phi(T) = \pi + \Delta$ (instead of $\phi(T) = \pi$). That is

$$\begin{aligned}
 |\Psi(T)\rangle &= c_0 |0\rangle \otimes \left[(d_0 + d_1) |C_\alpha^+\rangle + (d_0 - d_1) |C_\alpha^-\rangle \right] + \\
 &\quad c_1 |1\rangle \otimes \left[(d_0 + d_1) |C_{-\alpha e^{i\Delta}}^+\rangle + (d_0 - d_1) |C_{-\alpha e^{i\Delta}}^-\rangle \right]
 \end{aligned} \tag{25}$$

Now, $|C_{-\alpha e^{i\Delta}}^\pm\rangle = \pm e^{i\Delta} \hat{a}^\dagger |C_\alpha^\pm\rangle = \pm (1 + i\Delta \hat{a}^\dagger \hat{a} - \Delta^2 \hat{a}^\dagger \hat{a} \hat{a}^\dagger \hat{a} / 2 + \dots) |C_\alpha^\pm\rangle$, and for small Δ , only a few terms in the expansion are important. Below a threshold error $\Delta < \Delta_{\text{th}}$, the high-weight ($> \alpha^2/4$) terms exponentially decrease. The control error in this case only causes excitation of states in the pairwise quasi-degenerate manifold, which are subsequently corrected by two-photon dissipation. Note that during this autonomous correction, the cat states pick up an over-

all phase, depending on when the photon jump events happened, $|C_{-\alpha e^{i\Delta}}^\pm\rangle \rightarrow \pm e^{i\kappa} |C_\alpha^\pm\rangle$. Similar to Eq. 24, this extra phase leads to dephasing of the control cat qubit. In general, the threshold Δ_{th} depends on the strength of the Kerr nonlinearity and rate of two-photon dissipation. However, numerical and analytical estimates predict that in the experimentally relevant limit $K \gg \kappa_2$, the threshold is as large as $\Delta_{\text{th}} \sim \pi/6$ (see the Supplementary Materials). The large threshold shows the robustness of the gate to rotation errors.

Note that there is another source of rotation errors in the target cat. Any nondephasing error in the control qubit during the CX gate will cause leakage in the target oscillator. For example, a bit-flip error in the control cat at $t = T/2$ causes a phase-space rotation error in the target cat by $\pi/2$. That is, at the end of the gate, the target cat states are $|C_{i\alpha}^\pm\rangle$ rather than $|C_\alpha^\pm\rangle$. This can, however, be corrected by two-photon dissipation. Moreover, since the nondephasing errors in the control cat are exponentially suppressed, so is the leakage and the nondephasing faults from subsequent correction of leakage.

Hamiltonian of the bias-preserving CX gate

Having seen that the evolution in Eq. 19 results in a CX gate with biased-noise error channel, we will now present the physical interaction Hamiltonian required to implement it. In general, we assume that the amplitudes of the cats in the target and control oscillators, α and β , respectively, are different. The following time-dependent interaction Hamiltonian implements the bias-preserving CX between the two oscillators

$$\begin{aligned}
 \hat{H}_{\text{CX}} &= -K(\hat{a}_c^{\dagger 2} - \beta^2)(\hat{a}_c^2 - \beta^2) - \\
 &\quad K \left[\hat{a}_t^{\dagger 2} - \alpha^2 e^{-2i\phi(t)} \left(\frac{\beta - \hat{a}_c^\dagger}{2\beta} \right) - \alpha^2 \left(\frac{\beta + \hat{a}_c^\dagger}{2\beta} \right) \right] \\
 &\quad \times \left[\hat{a}_t^2 - \alpha^2 e^{2i\phi(t)} \left(\frac{\beta - \hat{a}_c}{2\beta} \right) - \alpha^2 \left(\frac{\beta + \hat{a}_c}{2\beta} \right) \right] - \\
 &\quad \frac{\dot{\phi}(t)}{4\beta} \hat{a}_t^\dagger \hat{a}_t \left(2\beta - \hat{a}_c^\dagger - \hat{a}_c \right)
 \end{aligned} \tag{26}$$

The first line in the above expression is the Hamiltonian of the parametrically driven nonlinear oscillator stabilizing the control cat qubit. The phase of the drive to this oscillator is fixed $\phi = 0$. To understand the other two lines, recall that $\hat{a}_c^\dagger, \hat{a}_c \sim \beta \hat{Z}_c \pm i\beta e^{-2\beta^2} \hat{Y}_c$. Therefore, if the control qubit is in the state $|0\rangle$ ($\sim |\beta\rangle$, for large β) and we ignore the exponentially small contribution from the term $\propto \hat{Y}_c$, then the above Hamiltonian is equivalent to

$$\hat{H}_{\text{CX}}^{|0\rangle_c} \equiv -K(\hat{a}_c^{\dagger 2} - \beta^2)(\hat{a}_c^2 - \beta^2) - K(\hat{a}_t^{\dagger 2} - \alpha^2)(\hat{a}_t^2 - \alpha^2) \tag{27}$$

Consequently, when the control qubit is in the state $|0\rangle$, the state of the target oscillator remains unchanged. On the other hand, if the control qubit is in the state $|1\rangle$ ($\sim |-\beta\rangle$, for large β), then Eq. 26 is equivalent to

$$\begin{aligned}
 \hat{H}_{\text{CX}}^{|1\rangle_c} &\equiv -K(\hat{a}_c^{\dagger 2} - \beta^2)(\hat{a}_c^2 - \beta^2) - \\
 &\quad K(\hat{a}_t^{\dagger 2} - \alpha^2 e^{-2i\phi(t)})(\hat{a}_t^2 - \alpha^2 e^{2i\phi(t)}) - \dot{\phi}(t) \hat{a}_t^\dagger \hat{a}_t
 \end{aligned} \tag{28}$$

From the second term of this expression, we see that the cat states $|C_{\alpha e^{i\phi(t)}}^{\pm}\rangle$ are the instantaneous eigenstates in the target oscillator. As a result, if the phase $\phi(t)$ changes adiabatically, respecting $\dot{\phi}(t) \ll |\Delta\omega_{\text{gap}}|$, then the orientation of the target cats follow $\phi(t)$, and α evolves in time to $\alpha e^{i\phi(t)}$. During this rotation in phase space, the target cat also acquires a geometric phase $\Phi_g^{\pm}(t)$ proportional to the area under the phase space path, $e^{i\Phi_g^{\pm}(t)}|C_{\alpha e^{i\phi(t)}}^{\pm}\rangle$, where $\Phi_g^{\pm}(t) = \phi(t) \alpha^2 r^{\mp 2}$. The difference in the two geometric phases, Φ_g^+ and Φ_g^- , reflects the fact that the mean photon numbers are different for the two states $|C_{\alpha e^{i\phi(t)}}^{\pm}\rangle$ and the area of the path followed by $|C_{\alpha e^{i\phi(t)}}^{\pm}\rangle$ in phase space is larger than that followed by $|C_{\alpha e^{i\phi(t)}}^{\pm}\rangle$. This geometric phase has some interesting properties, which are discussed in the Supplementary Materials. In the limit of large α , the difference in the two decreases exponentially in α^2 , $\Phi_g^+ - \Phi_g^- = 4\phi(t) \alpha^2 e^{-2\alpha^2} / (1 - e^{-4\alpha^2})$. Consequently, for large α , the state $|1\rangle \otimes d_0|C_{\alpha}^+\rangle + d_1|C_{\alpha}^-\rangle$ evolves in time to $e^{i\Phi_g(t)}|1\rangle \otimes d_0|C_{\alpha e^{i\phi(t)}}^+\rangle + d_1|C_{\alpha e^{i\phi(t)}}^-\rangle$, where $\Phi_g(t) = \Phi_g^+(t) - \Phi_g^-(t)$. That is, the geometric phase, effectively, is only an overall phase that results in an additional $Z_c(\Phi_g)$ rotation on the control qubit. This rotation can be accounted for in software or by an application of $Z_c(-\Phi_g)$ operation, or it can be directly cancelled during the CX gate itself by the addition of an additional interaction, given by the last term in Eq. 28. The projection of this term in the cat basis is given by

$$\hat{\phi}(t) \hat{a}_t^\dagger \hat{a}_t \equiv \hat{\phi}(t) \alpha^2 [r^2 |C_{\alpha e^{i\phi(t)}}^+\rangle \langle C_{\alpha e^{i\phi(t)}}^+| + r^{-2} |C_{\alpha e^{i\phi(t)}}^-\rangle \langle C_{\alpha e^{i\phi(t)}}^-|] \quad (29)$$

The above equation shows that the last term of Eq. 28 leads to a dynamic phase, which exactly cancels the geometric phase. As a result, we find that when the control cat is in state $|1\rangle$, an arbitrary state of the target qubit $d_0|C_{\alpha}^+\rangle + d_1|C_{\alpha}^-\rangle$ evolves in time to $d_0|C_{\alpha e^{i\phi(t)}}^+\rangle + d_1|C_{\alpha e^{i\phi(t)}}^-\rangle$. Consequently, the Hamiltonian in Eq. 26 leads to the evolution desired to implement the bias-preserving CX gate.

Numerically simulated noise channel of the CX gate

To show that the Hamiltonian of Eq. 26 does result in a bias-preserving CX, we first simulate Eq. 26 without noise in the oscillators. We chose $\alpha = \beta = 2$, $\phi(t) = \pi t/T$, and $T = 10/K$. Figure 3 shows the Pauli transfer matrix obtained in this way. The infidelity between the CX resulting from the evolution under Eq. 26 and an ideal CX is as small as $\sim 9.3 \times 10^{-7}$. This small infidelity, primarily resulting from nonadiabatic transitions due to finite KT , clearly shows that the Hamiltonian of Eq. 26 implements an ideal CX gate with an extremely high degree of accuracy.

Next, to account for losses we numerically simulate evolution under the master equation

$$\dot{\hat{\rho}} = -i[\hat{H}_{\text{CX}}, \hat{\rho}] + \kappa(n_{\text{th}} + 1) \sum_{i=c,t} \mathcal{D}[\hat{a}_i] \hat{\rho} + \kappa n_{\text{th}} \sum_{i=c,t} \mathcal{D}[\hat{a}_i^\dagger] \hat{\rho} \quad (30)$$

From this, we obtain the Pauli transfer matrix of the noisy CX, $R_{\text{noisy}}^{\text{CX}}$. The transfer matrix of the error channel is evaluated as $R_{\text{noise}} = R_{\text{noisy}}^{\text{CX}} (R_{\text{ideal}}^{\text{CX}})^{-1}$. Lastly, the error channel in the operator sum form is obtained from this transfer matrix. Instead of listing all the 256 matrix entries of the channel, we present its dominant terms. Moreover, to quantify the asymmetry in the noise channel of the CX gate, we introduce a quantity η referred to as the bias. The

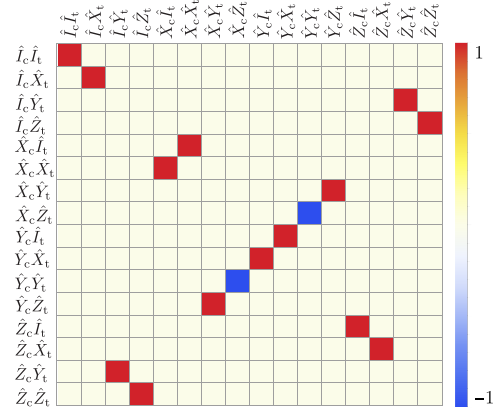


Fig. 3. Pauli transfer matrix of the CX gate. The transfer matrix is obtained by simulating the Hamiltonian in Eq. 26 with $\alpha = \beta = 2$, $\phi(t) = \pi t/T$, and $T = 10/K$. The infidelity of this CX operation with respect to an ideal two-level CX is 9.3×10^{-7} and results from nonadiabatic transitions due to finite KT .

bias, η , is defined as the ratio of probability of dephasing and nondephasing faults. The probability of dephasing errors is obtained from the error channel as the sum of the coefficients corresponding to the terms $\hat{I}_c \hat{Z}_t \hat{\rho} \hat{I}_c \hat{Z}_t$, $\hat{Z}_c \hat{I}_t \hat{\rho} \hat{Z}_c \hat{I}_t$, and $\hat{Z}_c \hat{Z}_t \hat{\rho} \hat{Z}_c \hat{Z}_t$. In the same way, the probability of nondephasing error is the sum of the coefficients corresponding to the remaining diagonal terms (except for $\hat{I}_c \hat{I}_t \hat{\rho} \hat{I}_c \hat{I}_t$). The coefficient corresponding to $\hat{I}_c \hat{I}_t \hat{\rho} \hat{I}_c \hat{I}_t$ yields the gate fidelity.

For $n_{\text{th}} = 0$, we find that the error channel is dominantly given by

$$\begin{aligned} \mathcal{E}(\hat{\rho}) \sim & \lambda_{I_c I_t, I_c I_t} \hat{I}_c \hat{I}_t \hat{\rho} \hat{I}_c \hat{I}_t + \lambda_{Z_c Z_t, Z_c Z_t} \hat{Z}_c \hat{Z}_t \hat{\rho} \hat{Z}_c \hat{Z}_t + \\ & \lambda_{Z_c I_t, Z_c I_t} \hat{Z}_c \hat{I}_t \hat{\rho} \hat{Z}_c \hat{I}_t + \lambda_{I_c Z_t, I_c Z_t} \hat{I}_c \hat{Z}_t \hat{\rho} \hat{I}_c \hat{Z}_t + \\ & (i\lambda_{I_c Z_t, Z_c I_t} \hat{I}_c \hat{Z}_t \hat{\rho} \hat{Z}_c \hat{I}_t + \text{h.c.}) \end{aligned} \quad (31)$$

For $\kappa = K/4000$, $T = 10/K$, and $\alpha = \beta = 2$, $\lambda_{I_c I_t, I_c I_t} \sim 0.94$, $\lambda_{Z_c Z_t, Z_c Z_t} \sim 0.029$, $\lambda_{I_c Z_t, I_c Z_t} \sim 0.015$, $\lambda_{Z_c I_t, Z_c I_t} \sim 0.015$, $\lambda_{I_c Z_t, Z_c I_t} \sim -0.009$, and the gate fidelity is 94%. The leakage is 9.6×10^{-7} , which does not notably increase from the case when losses are absent, and the bias is $\eta \sim 10^7$.

Next, we obtain the error channel for $n_{\text{th}} = 1\%$. To correct for leakage two-photon dissipation $\kappa_2 \mathcal{D}[\hat{a}^2] \hat{\rho}$ is added after the gate operation (see Methods for details). In the absence of the two-photon dissipation $\kappa_2 = 0$, the amount of leakage due to thermal photons is $\sim 3 \times 10^{-5}$. With $\kappa_2 = K/5$, leakage is reduced by almost two orders of magnitude to $\sim 5 \times 10^{-6}$. The gate fidelity in this case is reduced to $\sim 89\%$, and the error channel is dominantly given by

$$\begin{aligned} \mathcal{E}(\hat{\rho}) \sim & \lambda_{I_c I_t, I_c I_t} \hat{I}_c \hat{I}_t \hat{\rho} \hat{I}_c \hat{I}_t + \lambda_{Z_c Z_t, Z_c Z_t} \hat{Z}_c \hat{Z}_t \hat{\rho} \hat{Z}_c \hat{Z}_t + \\ & \lambda_{Z_c I_t, Z_c I_t} \hat{Z}_c \hat{I}_t \hat{\rho} \hat{Z}_c \hat{I}_t + \lambda_{I_c Z_t, I_c Z_t} \hat{I}_c \hat{Z}_t \hat{\rho} \hat{I}_c \hat{Z}_t + \\ & (i\lambda_{I_c I_t, Z_c I_t} \hat{I}_c \hat{I}_t \hat{\rho} \hat{Z}_c \hat{I}_t + \text{h.c.}) + \\ & (i\lambda_{I_c Z_t, Z_c I_t} \hat{I}_c \hat{Z}_t \hat{\rho} \hat{Z}_c \hat{I}_t + \text{h.c.}) \end{aligned} \quad (32)$$

with $\lambda_{I_c I_t, I_c I_t} \sim 0.89$, $\lambda_{Z_c Z_t, Z_c Z_t} \sim 0.052$, $\lambda_{I_c Z_t, I_c Z_t} \sim 0.016$, $\lambda_{Z_c I_t, Z_c I_t} \sim 0.038$, $\lambda_{I_c I_t, Z_c I_t} \sim -0.0002$, and $\lambda_{I_c Z_t, I_c Z_t} \sim -0.008$. The order of

magnitude of the other terms in the error channel is $\leq 10^{-5}$, and the bias is $\eta \sim 732$. When the size of the cats is increased to $\alpha = \beta = 2.2$ and $\alpha = \beta = 2.5$, the bias increases to $\eta \sim 902$ and $\eta \sim 3000$, respectively.

Lastly, we numerically estimate the error channel in case of over-rotation. This can happen, for example, when control errors lead to the gate being implemented for slightly longer time $T' = T + \delta(T)$. For the simulation, we choose $\pi\delta(T) = 0.01T$ corresponding to an over-rotation of the target cat by an angle $\Delta = 0.01$ (see Eq. 25). In this case, we simulate the master equation $\dot{\rho} = -i[\widehat{H}_{CX}, \rho] + \kappa D[\widehat{a}_c]\rho + \kappa D[\widehat{a}_t]\rho$ for time T' and then add two-photon dissipation $\kappa_2 D[\widehat{a}_t^2] + \kappa_2 D[\widehat{a}_c^2]$ to correct for overrotation. The dominant terms of the resulting error channel are

$$\begin{aligned} \mathcal{E}(\widehat{\rho}) \sim & \lambda_{I_t, I_c, I_t} \widehat{I}_c \widehat{I}_t \widehat{I}_c \widehat{I}_t + \lambda_{Z_t, Z_t, Z_t} \widehat{Z}_c \widehat{Z}_t \widehat{Z}_c \widehat{Z}_t + \\ & \lambda_{Z_t, Z_t, Z_t} \widehat{Z}_c \widehat{I}_t \widehat{Z}_c \widehat{I}_t + \lambda_{I_t, Z_t, Z_t} \widehat{I}_c \widehat{Z}_t \widehat{I}_c \widehat{Z}_t + \text{h.c.} \end{aligned} \quad (33)$$

For $\kappa = K/4000$, $\kappa_2 = K/5$, and $\alpha = \beta = 2$, $\lambda_{I_t, I_t, I_t} \sim 0.97$, $\lambda_{Z_t, Z_t, Z_t} \sim 0.038$, $\lambda_{I_t, Z_t, Z_t} \sim 0.015$, $\lambda_{Z_t, Z_t, Z_t} \sim 0.024$, $\lambda_{I_t, Z_t, Z_t} \sim -0.009$, and the bias is $\eta \sim 1955$. For $\alpha = \beta = 2.2$, the bias increases to $\eta \sim 2796$. The above examples confirm that the noise channel of the CX gate is biased, and the bias increases with the size of the cat. Because of the large Hilbert space size, it becomes difficult to perform numerical simulations for larger α . However, using the insights from single oscillator simulations in the presence of thermal and frequency noise (see the Supplementary Materials), we expect to achieve a bias of $\sim 10^4$ for $\alpha^2 < 10$ with experimentally reasonable experimental parameters.

Threshold and overhead for concatenation-based codes

To summarize the results so far, we have described the adiabatic preparation of the cat states $|C_{\alpha}^{\pm}\rangle$, $\mathcal{P}_{|\pm\rangle}$. We have also outlined the implementation of arbitrary rotations about the Z axis and implement ZZ(θ) gates. In addition, measurements along Z axis, $\mathcal{M}_{\widehat{Z}}$, can be performed using homodyne detection, while measurements along X axis, $\mathcal{M}_{\widehat{X}}$, require intermediary gates or ancilla (16, 20). The preparation operation, measurements and the gates Z(θ), and ZZ(θ) are trivially biased. However, we have shown that it is also possible to implement a biased-noise CX gate between two cat qubits. Observe that the bias-preserving set of unitaries {CX, Z(θ), ZZ(θ)} is not universal. As shown in the Supplementary Materials, no matter how the Hamiltonian evolution is constructed a native, universal set of bias-preserving unitaries is impossible. However, the unitaries {CX, Z(θ), ZZ(θ)}, in combination with state preparation, $\mathcal{P}_{|\pm\rangle}$, and measurements $\mathcal{M}_{\widehat{X}, \widehat{Z}}$ (20), are sufficient to implement universal fault-tolerant quantum computation (28). In this section, we will use the physical bias preserving set of operations

$$\{CX, Z(\theta), ZZ(\theta), \mathcal{P}_{|\pm\rangle}, \mathcal{M}_{\widehat{X}}, \mathcal{M}_{\widehat{Z}}\}$$

to realize efficient and compact circuits for fault-tolerant error correction based on concatenation (8) [(14) also discusses the repetition code using the idea of CX gates described here adapted to dissipative cats]. For the following analysis, we will consider the error channel in the Pauli-twirling approximation. That is, we ignore the off-diagonal elements in the error channel. This approximation can always be enforced by actively randomizing the Pauli frame at each step of a computation (2, 29). The resulting channel can then

be understood in the stochastic noise model by assigning a probability to each fault path. In this approximation, for example, the error channel of the two-qubit CX is dominantly of the form $\mathcal{E}(\widehat{\rho}) \sim \lambda_{I_t, I_c, I_t} (\widehat{I}_t \widehat{I}_c \widehat{I}_t \widehat{I}_c) + \lambda_{Z_t, Z_t, Z_t} (\widehat{Z}_t \widehat{Z}_c \widehat{Z}_t \widehat{Z}_c) + \lambda_{I_t, Z_t, Z_t} (\widehat{I}_t \widehat{Z}_c \widehat{I}_t \widehat{Z}_c) + \lambda_{Z_t, Z_t, I_t} (\widehat{Z}_t \widehat{I}_c \widehat{Z}_t \widehat{I}_c)$. This noise channel effectively introduces dephasing errors in the target and control cat qubits with probability $\lambda_{Z_t, Z_t, Z_t} + \lambda_{Z_t, Z_t, Z_t}$ and $\lambda_{I_t, Z_t, Z_t} + \lambda_{Z_t, Z_t, I_t}$, respectively. For simplicity, we will denote by ϵ the upper bound on the probability of a dephasing error in a cat qubit resulting from the noise during a single-qubit gate, two-qubit gate, state preparation, or measurement. For the example of the CX gate, this means that $\lambda_{Z_t, Z_t, Z_t} + \lambda_{Z_t, Z_t, I_t} \lambda_{I_t, Z_t, Z_t} + \lambda_{Z_t, Z_t, Z_t} \leq \epsilon$. We define a bias η so that the probability of a \widehat{X} or \widehat{Y} error is ϵ/η .

The idea introduced in (8) is to first encode the physical biased-noise qubits in a repetition code \mathcal{C}_1 and correct for dominant errors, in this case, phase flips. A repetition code with n qubits can correct $(n - 1)/2$ phase-flip errors. The code words are $|0\rangle_L = (|+\rangle_L + |-\rangle_L)/\sqrt{2}$ and $|1\rangle_L = (|+\rangle_L - |-\rangle_L)/\sqrt{2}$, where $|+\rangle_L = |C_{\alpha}^+\rangle |C_{\alpha}^+\rangle \dots$ and $|-\rangle_L = |C_{\alpha}^-\rangle |C_{\alpha}^-\rangle |C_{\alpha}^-\rangle \dots$. The result of the first encoding is a more symmetric noise channel with reduced noise strength. The repetition code with errors below a threshold can then be concatenated to a CSS code \mathcal{C}_2 to further reduce the errors. The \mathcal{C}_1 -protected \mathcal{C}_2 gadgets considered in (8) are {CX, $\mathcal{P}_{|0\rangle}$, $\overline{\mathcal{P}}_{|+\rangle}$, $\overline{\mathcal{M}}_{\widehat{X}}$, $\overline{\mathcal{M}}_{\widehat{Z}}$. In (8), these operations along with error correction are implemented using only trivially biased CZ gates, preparations, and measurements. Finally, the Clifford operations are supplemented with preparation of magic states $\overline{\mathcal{P}}_{|+\rangle}$ and $\overline{\mathcal{P}}_{|T\rangle}$. The error strengths at \mathcal{C}_1 is upper-bounded by the CX gadget (8). Here, we simplify the scheme for concatenated error correction using the physical bias-preserving gates for cat qubits {CX, ZZ(θ), Z(θ), $\mathcal{P}_{|\pm\rangle}$, $\mathcal{M}_{\widehat{X}}$, $\mathcal{M}_{\widehat{Z}}$. These operations are then used to implement the \mathcal{C}_1 -protected \mathcal{C}_2 gadgets {CX, $\mathcal{P}_{|0\rangle}$, $\mathcal{P}_{|+\rangle}$, $\mathcal{M}_{\widehat{X}}$, $\mathcal{M}_{\widehat{Z}}$. We show the circuit for the CX and error correction gadgets by exploiting the availability of the physical biased-noise CX gate between the cat qubits. Consequently, the error rate and volume of this CX gate are lower than that proposed in (8). Implementation of the other \mathcal{C}_1 -protected \mathcal{C}_2 Clifford operations is the same as in (8) and is outlined in the Supplementary Materials. We also complete the analysis by outlining the preparation of magic states using the trivially bias-preserving physical ZZ(θ) gates (10) in the Supplementary Materials.

Error correction in the repetition code

The $(n - 1)$ stabilizer generators for the repetition code are $\widehat{X}_1 \otimes \widehat{X}_2 \otimes \widehat{I}_3 \otimes \widehat{I}_4 \dots, \widehat{I}_1 \otimes \widehat{X}_2 \otimes \widehat{X}_3 \otimes \widehat{I}_4 \dots$, etc. The most naive way to detect errors is to measure each stabilizer generator using an ancilla as shown in Fig. 4A. Each ancilla is initialized in the state $|C_{\alpha}^+\rangle$. Then, two CX gates are implemented between the ancilla and qubits $j, j + 1$. Finally, the $(n - 1)$ ancillas are measured along the X axis $\mathcal{M}_{\widehat{X}}$. To be fault tolerant, each of the stabilizer generator is measured r times, and the syndrome bit is determined with a majority vote on the measurement outcomes. A syndrome bit is incorrect if $m \geq (r + 1)/2$ of the measurements are faulty.

This decoding scheme is equivalent to constructing an r -bit repetition code for each of the $(n - 1)$ stabilizer generators of the repetition code. Thus, each bit of syndrome from the inner code is itself encoded in an $[r, 1, r]$ repetition code so that decoding can proceed by first decoding the syndrome bits and then decoding the resulting syndrome. As we will see shortly, this naive way to decode the syndrome results in a simple analytic expressions for the logical error

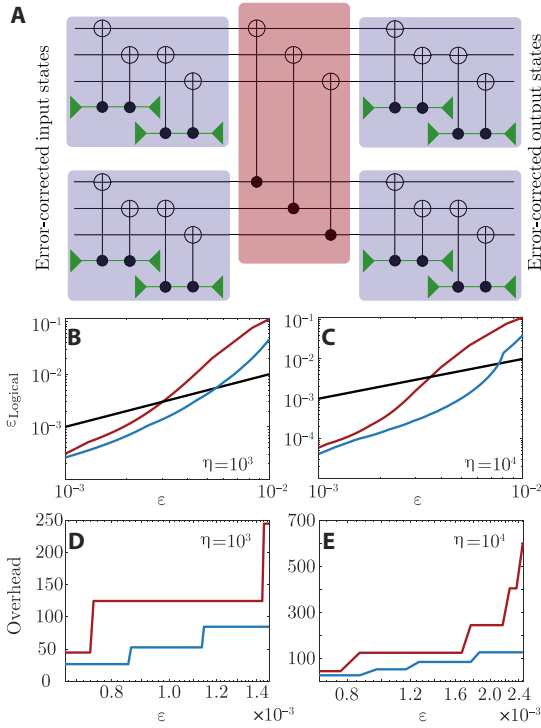


Fig. 4. Error correction and \overline{CX}_{cat} gadgets. (A) Each blue shaded block is an error correction gadget for a repetition code with $n = 3$. The black and green lines indicate code and ancilla qubits, respectively. The green triangles facing the left and right represent preparation and measurement of the ancilla, respectively. In the naive scheme, $(n - 1)$ stabilizer generators for the repetition code are measured using CX gates between pairs of data qubits and ancilla. Transversal CX gates between error-corrected code blocks (shown in the red shaded region) implement a \overline{CX}_{cat} operation. The code words are further error-corrected at the output. (B and C) Logical error rate for \overline{CX}_{cat} given in Eq. 38 (solid blue line) and from (8) (solid red line) for different bias η . The black line with slope = 1 is shown for reference. (D and E) Overhead of the \overline{CX}_{cat} gadget (blue line) for a target logical error rate of 0.67×10^{-3} (8, 28). The overhead for the gadget proposed in (8) for the same target error rate is shown in red.

rates. However, it is by no means an ideal approach to decode, and one can imagine that the two-stage decoder above could be replaced by one that directly infers the most likely error on the n -qubit repetition code, given that s measured syndrome bits. In a few sections, we will explain the notion of a measurement code that exploits these insights to improve on the naive scheme by constructing a block code that can directly correct the bit-flip errors on the n data qubits in a single decoding step.

Logical CX gate (or \overline{CX}) with naive decoding

Since a physical CX with error channel biased toward dephasing errors is available, the \overline{CX} gadget can be implemented with transversal CXs between two code blocks, as shown in Fig. 4A. We will refer to this as \overline{CX}_{cat} gadget, because the biased-noise CX gates are realized using cat qubits. We will now estimate an upper bound for the logical error rate of the \overline{CX}_{cat} gadget.

Each data qubit coming into the target and control blocks of the \overline{CX}_{cat} gadget is subject to $2r$ CX gates during the previous error correction step. The probability of a dephasing fault in each data

qubit is therefore $2r\epsilon$. Next, each data qubit in the target and control block is subject to one CX gate. Note, however, that phase errors from the target can spread to phase errors on the control. Therefore, the probability of a dephasing fault in each qubit in the target and control blocks is $2r\epsilon + \epsilon$ and $4r\epsilon + \epsilon$, respectively. A logical error will occur if $m \geq (n + 1)/2$ qubits in the target or control blocks are faulty. Therefore, the probability of a logical error in the control and target blocks before they are input into the error correction gadgets are

$$\epsilon_{target} \leq \binom{n}{\frac{n+1}{2}} (2r\epsilon + \epsilon)^{(n+1)/2}, \epsilon_{control} \leq \binom{n}{\frac{n+1}{2}} (4r\epsilon + \epsilon)^{(n+1)/2} \tag{34}$$

Each of the error correction gadgets now measure $(n - 1)$ syndromes, and each syndrome bit must be read correctly for successful decoding. Each syndrome bit is measured r times and requires two CX gates between a pair of code qubits and an ancilla. A syndrome measurement can be incorrect if the preparation or measurement of the ancilla was incorrect or if there was a dephasing error on the ancilla during the CXs. Therefore, an upper bound on the probability of error due to failure of the error correction in the target and control blocks is

$$\epsilon_{ec} \leq 2(n - 1) \binom{r}{\frac{r+1}{2}} (4\epsilon)^{(r+1)/2} \tag{35}$$

In the worst case, a single nondephasing error occurring with probability ϵ/η anywhere in the circuit will cause the failure of the gadget. There are $4(n - 1)r$ CX gates in each of the error correction gadgets at the input and output and n transversal CX gates. As a result, the probability of an error due to a nondephasing fault is

$$\epsilon' \leq (8(n - 1)r + n) \frac{\epsilon}{\eta} \tag{36}$$

Finally, the probability of a logical error in the \overline{CX} gadget is given by

$$\epsilon_{cat} = \epsilon_{target} + \epsilon_{control} + \epsilon_{ec} + \epsilon' \tag{37}$$

$$= \binom{n}{\frac{n+1}{2}} (2r\epsilon + \epsilon)^{(n+1)/2} + \binom{n}{\frac{n+1}{2}} (4r\epsilon + \epsilon)^{(n+1)/2} + 2(n - 1) \binom{r}{\frac{r+1}{2}} (4\epsilon)^{(r+1)/2} + (8(n - 1)r + n) \frac{\epsilon}{\eta} \tag{38}$$

Figure 4 (B and C) compares the logical error rates for the \overline{CX}_{cat} gadget in Eq. 38 (blue line) and that for the gadget in (8) (red line) as a function of the bare error ϵ for different bias η . For reference, a line with slope = 1 is also shown (black). The \overline{CX}_{cat} gadget clearly has lower probability for logical errors. For $\eta = 10^4$, the threshold error for the gadget (that is, where the blue curve intersects the black line) is $\epsilon_{cat} = 7.5 \times 10^{-3}$. This is more than twice the threshold of the CX gadget in (8), $\epsilon_{AP} = 3.55 \times 10^{-3}$. For smaller bias, the contribution from the nondephasing term in Eq. 38 takes over, and the performance of \overline{CX} degrades.

Moreover, we find that the \overline{CX}_{cat} gadget also requires less overhead to reach the same target logical error rate compared to the

gadget in (8). To demonstrate this, we estimate the circuit volume required to reach a target error rate of 0.67×10^{-3} . Using Eqs. 38, we find the n and r required so that $\epsilon_{\text{cat}} \leq 0.67 \times 10^{-3}$. The circuit volume for the $\overline{\text{CX}}$ in (8) and that described here are $7nr$ and $8(n-1)r + 2n$, respectively. Figure 4 (D and E) compares these overheads for $\eta = 10^3$ and $\eta = 10^4$, as a function of ϵ . The $\overline{\text{CX}}_{\text{cat}}$ described here has a smaller overhead. For example, with $\epsilon = 2.5 \times 10^{-3}$ and $\eta = 10^4$, the overhead for $\overline{\text{CX}}_{\text{cat}}$ is ~ 5 times smaller than that for the gadget described in (8).

Recall that in the approach described above, the repetition code is concatenated with a CSS code. Therefore, ϵ_{cat} must be lower than the accuracy threshold for a CSS code for computation with arbitrarily high accuracy to be possible. For the example of the CSS code construction in (9, 28), the lower bound on the accuracy threshold is $\epsilon_{\text{CSS}}^{\text{th}} = 0.67 \times 10^{-3}$. We find that for $\eta = 10^4$, $n = 0.0043$, $n = 19$, and $r = 7$ for $\epsilon_{\text{cat}} = 0.67 \times 10^{-3}$. In addition, in the Supplementary Materials, we show that magic-state preparation and distillation is also possible for $\epsilon \leq 0.0043$. Therefore, $\epsilon = 0.0043$ is a lower bound on the accuracy threshold for universal computation for $\eta = 10^4$, which is approximately two times larger than that in (9). The numerical simulations for the CX gate outlined in the earlier section suggest that it is possible to achieve bias in the range $\eta \sim 10^3 - 10^4$ for cats with average photon numbers between $\bar{n} = 5 - 10$. The challenge is then to achieve physical dephasing rate below the threshold, which is not very large for the concatenated scheme discussed here (0.43% for $\eta = 10^4$). It will be hard to achieve these small error rates in current experimental setups even if large biases could be achieved. In contrast, surface codes tailored to biased noise qubits provide means to achieve ultrahigh thresholds. A recent work (30) estimated a threshold of $>5\%$ for the tailored surface code for biases $\eta \gtrsim 100$ under a phenomenological noise model, provided that native bias-preserving CX gates are available. The modest target of physical error rates below 5% and biases greater than 100 is far more realistic for current experimental setups.

Fault tolerance with a measurement code

As we discussed in the earlier section, the naive way to decode by measuring $(n-1)$ stabilizer generators is suboptimal. We will now discuss how we can improve decoding by using what we refer to as, a measurement code. To construct a measurement code, we desire that our syndrome measurement procedure measures a total of s elements of the stabilizer group (not necessarily the specified generators) by coupling to ancillas and that it can correct any $t = (d-1)/2$ phase-flip errors on the n qubits. That is, we wish to have a classical code with parameters $[n+s, n, d]$. However, not every classical code with those parameters is admissible, because the classical parity checks must still be compatible with the stabilizers of the original quantum code, in this case, the repetition code. In particular, each parity check in the measurement code must have even weight when restricted to the data qubits so that it commutes with the logical \hat{Z}_L operator of the quantum phase-flip code. Consistency with the stabilizer group of the base quantum code is the only constraint on a measurement code. There has been some work in the past few years, which indicates that either measuring redundant stabilizers or using the large amount of redundancy already in the code can make the code tolerant to measurement errors (31–33). The measurement code, presented here, identifies a classical error correcting code to protect against measurement errors and provides an intuitive way to calculate the optimal number of syndrome measure-

ments for a desired code distance. This idea is also referred to as the quantum data syndrome codes in (34–36).

The general form of a measurement code can be specified by the parity check matrix H_M . This, in turn, is specified as a function of the (generally redundant) parity checks H_Z of the quantum repetition code and an additional set of s ancilla bits that label the measurements. Given H_Z , the parity check matrix of the measurement code is the block matrix

$$H_M = (H_Z I_s) \tag{39}$$

where I_s is the $s \times s$ identity matrix. Since there are s ancilla bits for readout, H_M is an $s \times (n+s)$ matrix. The fact that the rows of H_Z come from the stabilizers of a quantum repetition code is captured by the constraint that they must all have even weight. The rows are clearly linearly independent, so the associated code has parameters $[n+s, n, d]$ for some $d \leq n$. The distance is never greater than n since a string of \hat{Z} operators on the data qubits, corresponding to 1's on exactly the first n bits, is always in the kernel of H_M .

The measurement of the j th parity check in the measurement code can be performed by a standard choice of circuit. We simply apply a CX gate to qubit i if there is a 1 in column i and target the ancilla labeled in column $n+j$. Note that by construction there is always a 1 in position $(j, n+j)$ of H_M . The effective error rate of this bare-ancilla measurement gadget will depend on the number of CX gates used and, hence, on the weight of the stabilizer being measured. Therefore, all other things (such as code distance) being equal, lower weight rows are preferred when designing a measurement code. Note that it is possible that the redundant stabilizers to be measured are higher weight or more nonlocal than the stabilizer generators themselves (see for example Eq. 41). In practice, because of experimental constraints, it may become more difficult to measure higher-weight/nonlocal stabilizers. However, this may be a vital tool to demonstrate fault-tolerant error correction and better than breakeven performance in near-term experiments.

The two examples we consider here are generated from the following choices for H_Z , displayed here in transpose to save space

$$H_Z^T = \begin{pmatrix} 1 & 1 & 0 \\ 1 & 0 & 1 \\ 0 & 1 & 1 \end{pmatrix} \tag{40}$$

$$H_Z^T = \begin{pmatrix} 1 & 0 & 0 & 0 & 1 & 1 & 0 & 0 & 1 \\ 1 & 1 & 0 & 0 & 0 & 0 & 1 & 1 & 0 \\ 0 & 1 & 1 & 0 & 0 & 1 & 0 & 1 & 0 \\ 0 & 0 & 1 & 1 & 0 & 0 & 0 & 1 & 1 \\ 0 & 0 & 0 & 1 & 1 & 0 & 1 & 1 & 0 \end{pmatrix} \tag{41}$$

These codes were chosen to saturate the distance bound, so $d = n$ for each code (so $d = 3$ and $d = 5$, respectively). These were found by guess work, and no attempt at finding optimal measurement codes was made, although these are the best of the few that were tested. To contrast our choices with the choice associated with repeating the measurements of the standard generators r times for $n = r = 3$, the measurement code is specified by

$$H_Z^T = \begin{pmatrix} 1 & 1 & 1 & 0 & 0 & 0 \\ 1 & 1 & 1 & 1 & 1 & 1 \\ 0 & 0 & 0 & 1 & 1 & 1 \end{pmatrix} \tag{42}$$

Both this choice and the $n = 3$ choice in Eq. 40 have distance $d = 3$ as measurement codes. However, our choice corresponds to a $[6,3,3]$ measurement code, whereas the naive repeated generator method yields a $[12,3,3]$ measurement code. In general, the naive scheme yields a $[n + (n - 1)r, n, d(n, r)]$ code, and for smaller r , the distance will not yet saturate to n . For $n = 5$, we need $r = 2$ before the measurement code has distance 3 and $r = 4$ before the distance saturates at $d = 5$. Thus, the naive scheme yields either a $[13,5,3]$ code or a $[21,5,5]$ code, which are inferior in either distance or rate, respectively, to the $[14,5,5]$ code that results from the choice in Eq. 41.

These examples also illustrate a counterintuitive feature of measurement codes. Consider again the naive repeated generator method with $n = 5$ and $r = 2$ or 4. If the decoder works by first decoding the syndrome bits individually, then the data are only protected against at most $(r - 1)/2 = 0$ or 1 arbitrary errors, respectively. However, a decoder that uses the structure of the associated measurement code can correct 1 or 2 arbitrary data errors with these respective parameters, which then reduces the leading order behavior of the code failure probability.

Both of the above codes in Eqs. 40 and 41 are small enough that the exact probability of a decoding failure can be computed via an exhaustive lookup table. To demonstrate the advantage of the measurement code over naive encoding and decoding, we estimate the probability of a logical error in the CX gadget using the measurement code in Eq. 41 for $n = 5$. The corresponding threshold is $\sim 6 \times 10^{-3}$. On the other hand, to reach a similar threshold using the naive decoder requires $n = 11, r = 5$. The optimal decoder requires fewer resources than the naive decoder. In general, this optimal (maximum-

likelihood) decoder is infeasible to implement because it requires exponential resources in n and s to compute, so substantially, larger codes will need decoding heuristics such as message-passing algorithms to approach peak decoding performance. The decoder declares failure whenever the data error is not guessed exactly right, although this is not strictly speaking necessary. When repeated rounds of error correction occur, it is sufficient to define success as reducing the weight of any correctable error. This more relaxed definition is harder to analyze, however, so our stricter definition of failure is used in all of the threshold calculations.

DISCUSSION

Here, we have presented a driven cat qubit with highly biased noise channel and shown how to perform a CX gate, which preserves the error bias. A bias-preserving CX gate with strictly two-dimensional systems is impossible (8, 14). We are able to circumvent this no-go conjecture by exploiting the phase space topology of the underlying continuous variable system.

The physical realization of the CX gate requires a three-wave mixing between the oscillators. The natural coupling between two oscillators is, however, beam-splitter type. Fortunately, the oscillators are themselves fourth-order Kerr nonlinear. Thus, the required three-wave mixing can be generated by parametrically driving the target oscillator at a frequency ω_d such that $\omega_d = 2\omega_t - \omega_c$. Here, ω_t and ω_c are the frequencies of the target and control oscillators, respectively. When this condition is satisfied, the fourth-order nonlinearity converts a photon in the drive and a photon in the control to two photons in the target. Thereby, an effective three-wave mixing is realized between the control and target. The Kerr nonlinearity of the oscillators themselves is sufficient to realize the CX interaction Hamiltonian, and no additional coupling elements are necessary. Moreover, because of the parametric nature, the coupling is controllable. A possible realization of the CX gate Hamiltonian in superconducting circuits is shown in Fig. 5. It is feasible to extend the scheme for the CX gate to implement a bias-preserving controlled-controlled-NOT (CCX) gate between three cat qubits. A naive circuit would, however, require a controllable four-wave mixing between the oscillators that is typically much weaker. As described in the Supplementary Materials, it is possible to implement a bias-preserving CCX gate using only three-wave mixing and four cat qubits. To summarize, the bias-preserving set of unitaries discussed in this paper, which are also physically implementable with three-wave mixing (or less), is $\{CX, CCX, ZZ(\theta), Z(\theta), CCZ\}$. These can be supplemented with state preparations $\mathcal{P}_{|\pm\rangle}$ and measurements $\mathcal{M}_{\hat{X}, \hat{Z}}$ for universal fault-tolerant quantum computation.

Furthermore, by adapting the scheme for concatenated error correction in (8), we have demonstrated that having bias-preserving CX gates leads to substantial improvements in fault-tolerant thresholds and overheads. At the level of repetition code, the estimated bound for fault-tolerant thresholds with naive decoding and experimentally reasonable biases of $\sim 10^3 - 10^4$ is $\sim 0.55\% = 0.75\%$. Consequently, high-quality oscillators will still be required so that the phase-flip error remains small enough. One way to improve the threshold is by using better decoding techniques, for example, by using the measurement code. The approach based on concatenating a repetition code to another CSS code is not necessary or ideal. A more efficient technique would be to directly implement a code tailored to asymmetric noise such as the surface code (12, 13) or cyclic

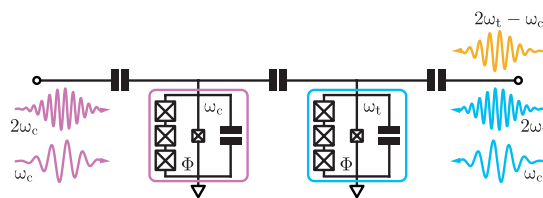


Fig. 5. Schematic for possible realization of the bias-preserving CX gate with superconducting circuits. Here, the Kerr nonlinear oscillators (of frequencies ω_t and ω_c) are implemented with superconducting nonlinear asymmetric inductive elements or SNAILs (38, 39). A SNAIL can be biased with an external magnetic field so that it has both three- and four-wave mixing capabilities. It can therefore be used to implement the two-photon driven Kerr nonlinear oscillator and realize a cat qubit with biased-noise channel (19). The Hamiltonian in Eq. 26 can be simplified as $\hat{H} = -K\hat{a}_c^{\dagger 2}\hat{a}_c^2 - K\hat{a}_t^{\dagger 2}\hat{a}_t^2 + K\beta^2(\hat{a}_c^{\dagger 2} + \text{h.c.}) + K\alpha^2 \cos(\phi(t)) (e^{i\phi(t)}\hat{a}_t^{\dagger 2} + \text{h.c.}) - (K\alpha^2 \sin(\phi(t))/\beta) (ie^{i\phi(t)}\hat{a}_t^{\dagger 2}\hat{a}_c + \text{h.c.}) + (K\alpha^4/2\beta) \sin(2\phi(t)) (i\hat{a}_c^{\dagger} + \text{h.c.}) - (K\alpha^4 \sin^2(\phi(t))/\beta^2)\hat{a}_c^{\dagger}\hat{a}_c - \phi(t)\hat{a}_t^{\dagger}\hat{a}_t/2 + (\phi(t)/4\beta)\hat{a}_t^{\dagger}\hat{a}_t(\hat{a}_c^{\dagger} + \text{h.c.})$. By expressing the Hamiltonian in this form, the drives required to realize the Hamiltonian become immediately clear. First, a drive to the control cavity (fixed amplitude and phase) centered at $2\omega_c$ is required for the two-photon term driving the control cavity via three-wave mixing. Next, a drive to the target cavity with time-dependent amplitude at $2\omega_t$ results in the two-photon term driving the target cavity via three-wave mixing. An additional drive $2\omega_t - \omega_c$ (time-dependent amplitude and phase) is applied to the target cavity to realize the coupling terms $\propto \hat{a}_t^{\dagger}\hat{a}_c$ in Eq. 26. A drive applied directly to the control cavity centered at ω_c with time-dependent phase and amplitude realizes the single-photon drive to the control cavity. A final drive to the target cavity at ω_c with time-dependent amplitude and phase realizes the last term in the Hamiltonian (40).

code (11) with the cat qubit. An analysis of these codes tailored to the cat qubits will be carried out in future work.

METHODS

Error channel from simulations

Here, we describe how the error channel in the sections titled “Thermal bath with white-noise spectrum” and “Numerically simulated noise channel of the CX gate” is extracted from master equation simulations. The dimension of the system of s cat qubits is $d = 2^s$, and the elements of the Pauli transfer matrix R are

$$R_{ij} = \frac{1}{d} \text{Tr}[\hat{P}_i \mathcal{E}(\hat{P}_j)] \quad (43)$$

In the above expression, $\mathcal{E}(\cdot)$ is the error channel, and \hat{P}_i is the d^2 Pauli operators. The Pauli transfer matrix at time t is extracted by simulating the master equation, using the software package QuTiP (37), with the Pauli operators as initial state at $t = 0$. Once the $d^2 \times d^2$ elements of the Pauli transfer matrix are obtained, the above equation is inverted to obtain the error channel.

CX gate in the presence of thermal noise

The error channel of the CX gate in the presence of thermal noise was given in the section titled “Numerically simulated noise channel of the CX gate.” The channel is obtained from the transfer matrix, which itself is obtained in two steps. First, the master equation for the CX, $\dot{\hat{\rho}} = -i[\hat{H}_{\text{CX}}, \hat{\rho}] + \sum_{ic,t} \kappa(1 + n_{\text{th}}) \mathcal{D}[\hat{a}_i] \hat{\rho} + \kappa n_{\text{th}} \mathcal{D}[\hat{a}_i^\dagger] \hat{\rho}$, is simulated for time $T = 10/K$ with $\phi(t) = \pi t/T$, $\alpha = \beta = 2$, and Pauli matrices as the input. Here, $i = c, t$. Next, all the interactions between the control and target oscillators are removed, and the Hamiltonian of the system is set to that two uncoupled oscillators $\hat{H}' = -K [\sum_i \hat{a}_i^\dagger \hat{a}_i + \alpha^2 (\hat{a}_i^{\dagger 2} + \hat{a}_i^2)]$. Now, the master equation with two-photon dissipation is simulated, $\dot{\hat{\rho}} = -i[\hat{H}', \hat{\rho}] + \sum_{ic,t} \kappa(1 + n_{\text{th}}) \mathcal{D}[\hat{a}_i] \hat{\rho} + \kappa n_{\text{th}} \mathcal{D}[\hat{a}_i^\dagger] \hat{\rho} + \kappa_2 \mathcal{D}[\hat{a}_i^2] \hat{\rho}$, for time $T' = 2/\kappa_2$ and using the density matrix from the output of the CX simulation as the input. The transfer matrix from the second simulation is inverted to obtain the error channel.

As shown by Eq. 25, two-photon dissipation on the target oscillator $\mathcal{D}[\hat{a}_i^2]$ during the CX gate introduces additional phase-flip errors in the control oscillator. This implies that, although the two-photon dissipation corrects leakage, it will also reduce the gate fidelity. It is possible to overcome this problem by adding time-dependent, correlated dissipation between the control and target oscillators. However, the numerical simulations become notably harder. To avoid this, we use the two-step process discussed above.

SUPPLEMENTARY MATERIALS

Supplementary material for this article is available at <http://advances.sciencemag.org/cgi/content/full/6/34/eaay5901/DC1>

REFERENCES AND NOTES

1. P. Aliferis, D. Gottesman, J. Preskill, Accuracy threshold for postselected quantum computation. *Quant. Inf. Comput.* **8**, 181–244 (2008).
2. E. Knill, Quantum computing with realistically noisy devices. *Nature* **434**, 39–44 (2005).
3. R. Raussendorf, J. Harrington, K. Goyal, Topological fault-tolerance in cluster state quantum computation. *New J. Phys.* **9**, 199 (2007).
4. I. M. Pop, K. Geerlings, G. Catelani, R. J. Schoelkopf, L. I. Glazman, M. H. Devoret, Coherent suppression of electromagnetic dissipation due to superconducting quasiparticles. *Nature* **508**, 369–372 (2014).
5. M. D. Shulman, O. E. Dial, S. P. Harvey, H. Bluhm, V. Umansky, A. Yacoby, Demonstration of entanglement of electrostatically coupled singlet-triplet qubits. *Science* **336**, 202–205 (2012).
6. T. Watson, S. G. J. Philips, E. Kawakami, D. R. Ward, P. Scarlino, M. Veldhorst, D. E. Savage, M. G. Lagally, M. Friesen, S. N. Coppersmith, M. A. Eriksson, L. M. K. Vandersypen, A programmable two-qubit quantum processor in silicon. *Nature* **555**, 633–637 (2018).
7. G. Waldherr, Y. Wang, S. Zaiser, M. Jamali, T. Schulte-Herbrüggen, H. Abe, T. Ohshima, J. Isoya, J. F. Du, P. Neumann, J. Wrachtrup, Quantum error correction in a solid-state hybrid spin register. *Nature* **506**, 204–207 (2014).
8. P. Aliferis, J. Preskill, Fault-tolerant quantum computation against biased noise. *Phys. Rev. A* **78**, 052331 (2008).
9. P. Aliferis, F. Brito, D. P. DiVincenzo, J. Preskill, M. Steffen, B. M. Terhal, Fault-tolerant computing with biased-noise superconducting qubits: A case study. *New J. Phys.* **11**, 013061 (2009).
10. P. Webster, S. D. Bartlett, D. Poulin, Reducing the overhead for quantum computation when noise is biased. *Phys. Rev. A* **92**, 062309 (2015).
11. A. Robertson, C. Granade, S. D. Bartlett, S. T. Flammia, Tailored codes for small quantum memories. *Phys. Rev. Applied* **8**, 064004 (2017).
12. D. K. Tuckett, S. D. Bartlett, S. T. Flammia, Ultrahigh error threshold for surface codes with biased noise. *Phys. Rev. Lett.* **120**, 050505 (2018).
13. D. K. Tuckett, A. S. Darmawan, C. T. Chubb, S. Bravyi, S. D. Bartlett, S. T. Flammia, Tailoring surface codes for highly biased noise. *Phys. Rev. X* **9**, 041031 (2019).
14. J. Guillaud, M. Mirrahimi, Repetition cat-qubits for fault-tolerant quantum computation. *Phys. Rev. X* **9**, 041053 (2019).
15. S. Puri, S. Boutin, A. Blais, Engineering the quantum states of light in a Kerr-nonlinear resonator by two-photon driving. *npj Quantum Inf.* **3**, 18 (2017).
16. N. Ofek, A. Petrenko, R. Heeres, P. Reinhold, Z. Leghtas, B. Vlastakis, Y. Liu, L. Frunzio, S. M. Girvin, L. Jiang, M. Mirrahimi, M. H. Devoret, R. J. Schoelkopf, Extending the lifetime of a quantum bit with error correction in superconducting circuits. *Nature* **536**, 441–445 (2016).
17. Z. Leghtas, S. Touzard, I. M. Pop, A. Kou, B. Vlastakis, A. Petrenko, K. M. Sliwa, A. Narla, S. Shankar, M. J. Hatridge, M. Reagor, L. Frunzio, R. J. Schoelkopf, M. Mirrahimi, M. H. Devoret, Confining the state of light to a quantum manifold by engineered two-photon loss. *Science* **347**, 853–857 (2015).
18. S. Touzard, A. Grimm, Z. Leghtas, S. O. Mundhada, P. Reinhold, C. Axline, M. Reagor, K. Chou, J. Blumoff, K. M. Sliwa, S. Shankar, L. Frunzio, R. J. Schoelkopf, M. Mirrahimi, M. H. Devoret, Coherent oscillations inside a quantum manifold stabilized by dissipation. *Phys. Rev. X* **8**, 021005 (2018).
19. A. Grimm, N. E. Frattini, S. Puri, S. O. Mundhada, S. Touzard, M. Mirrahimi, S. M. Girvin, S. Shankar, M. H. Devoret, The Kerr-Cat Qubit: Stabilization, Readout, and Gates. *Nature* **584**, 205–209 (2020).
20. S. Puri, A. Grimm, P. Campagne-Ibarcq, A. Eickbusch, K. Noh, G. Roberts, L. Jiang, M. Mirrahimi, M. H. Devoret, S. M. Girvin, Stabilized cat in driven nonlinear cavity: A fault-tolerant error syndrome detector. *Phys. Rev. X* **9**, 041009 (2019).
21. H. Goto, Universal quantum computation with a nonlinear oscillator network. *Phys. Rev. A* **93**, 050301 (2016).
22. M. Mirrahimi, Z. Leghtas, V. V. Albert, S. Touzard, R. J. Schoelkopf, L. Jiang, M. H. Devoret, Dynamically protected cat-qubits: A new paradigm for universal quantum computation. *New J. Phys.* **16**, 045014 (2014).
23. J. Cohen, W. C. Smith, M. H. Devoret, M. Mirrahimi, Degeneracy-preserving quantum nondemolition measurement of parity-type observables for cat qubits. *Phys. Rev. Lett.* **119**, 060503 (2017).
24. Y. Y. Gao, B. J. Lester, Y. Zhang, C. Wang, S. Rosenblum, L. Frunzio, L. Jiang, S. M. Girvin, R. J. Schoelkopf, Programmable interference between two microwave quantum memories. *Phys. Rev. X* **8**, 021073 (2018).
25. R. C. Bialczak, R. McDermott, M. Ansmann, M. Hofheinz, N. Katz, E. Lucero, M. Neeley, A. D. O’Connell, H. Wang, A. N. Cleland, J. M. Martinis, 1/f flux noise in josephson phase qubits. *Phys. Rev. Lett.* **99**, 187006 (2007).
26. D. Sank, R. Barends, R. C. Bialczak, Y. Chen, J. Kelly, M. Lenander, E. Lucero, M. Mariantoni, A. Megrant, M. Neeley, P. J. J. O’Malley, A. Vainsencher, H. Wang, J. Wenner, T. C. White, T. Yamamoto, Y. Yin, A. N. Cleland, J. M. Martinis, Flux noise probed with real time qubit tomography in a josephson phase qubit. *Phys. Rev. Lett.* **109**, 067001 (2012).
27. D. F. Walls, G. J. Milburn, *Quantum Optics* (Springer Science & Business Media, 2007).
28. P. Aliferis, J. Preskill, Fibonacci scheme for fault-tolerant quantum computation. *Phys. Rev. A* **79**, 012332 (2009).
29. J. J. Wallman, J. Emerson, Noise tailoring for scalable quantum computation via randomized compiling. *Phys. Rev. A* **94**, 052325 (2016).
30. D. K. Tuckett, S. D. Bartlett, S. T. Flammia, B. J. Benjamin, Fault-tolerant thresholds for the surface code in excess of 5% under biased noise. *Phys. Rev. Lett.* **124**, 130501 (2020).

31. Y. Fujiwara, Ability of stabilizer quantum error correction to protect itself from its own imperfection. *Phys. Rev. A* **90**, 062304 (2014).
32. E. T. Campbell, A theory of single-shot error correction for adversarial noise. *Quant. Sci. Tech.* **4**, 025006 (2019).
33. V. N. Premakumar, H. Sha, D. Crow, E. Bach, R. Joynt, 2-designs and redundant syndrome extraction for quantum error correction. arXiv:1907.04497 [quant-ph] (10 July 2019).
34. A. Ashikhmin, C.-Y. Lai, T. A. Brun, Robust quantum error syndrome extraction by classical coding, in *2014 IEEE International Symposium on Information Theory (IEEE, 2014)*, pp. 546–550.
35. A. Ashikhmin, C.-Y. Lai, and T. A. Brun, Correction of data and syndrome errors by stabilizer codes, in *2016 IEEE International Symposium on Information Theory (IEEE, 2016)*, pp. 2274–2278.
36. A. Ashikhmin, C.-Y. Lai, and T. A. Brun, Quantum data syndrome codes. arXiv:1907.01393 [quant-ph] (2 July 2019).
37. J. R. Johansson, P. D. Nation, F. Nori, QuTiP: An open-source python framework for the dynamics of open quantum systems. *Comput. Phys. Commun.* **183**, 1760–1772 (2012).
38. N. E. Frattini, U. Vool, S. Shankar, A. Narla, K. M. Sliwa, M. H. Devoret, 3-wave mixing josephson dipole element. *Appl. Phys. Lett.* **110**, 222603 (2017).
39. N. E. Frattini, V. V. Sivak, A. Lingenfelter, S. Shankar, M. H. Devoret, Optimizing the nonlinearity and dissipation of a SNAIL parametric amplifier for dynamic range. *Phys. Rev. Applied* **10**, 054020 (2018).
40. S. Touzard, A. Kou, N. E. Frattini, V. V. Sivak, S. Puri, A. Grimm, L. Frunzio, S. Shankar, M. H. Devoret, Gated conditional displacement readout of superconducting qubits. *Phys. Rev. Lett.* **122**, 080502 (2019).
41. M. Dykman, *Fluctuating Nonlinear Oscillators: From Nanomechanics to Quantum Superconducting Circuits* (Oxford Univ. Press, 2012).
42. S. Puri, C. K. Andersen, A. L. Grimsmo, A. Blais, Quantum annealing with all-to-all connected nonlinear oscillators. *Nat. Commun.* **8**, 15785 (2017).
43. M. V. Berry, Quantal phase factors accompanying adiabatic changes. *Proc. R. Soc. Lond. A* **392**, 45–57 (1984).
44. S. Chaturvedi, M. S. Sriram, V. Srinivasan, Berry's phase for coherent states. *J. Phys. A* **20**, L1071 (1987).
45. S. M. Girvin, K. Yang, *Modern Condensed Matter Physics* (Cambridge Univ. Press, 2019).
46. S. Bravyi, A. Kitaev, Universal quantum computation with ideal clifford gates and noisy ancillas. *Phys. Rev. A* **71**, 022316 (2005).

Acknowledgments: We thank I. Chuang, A. L. Grimsmo, A. Darmawan, and M. Mirrahimi for discussions. **Funding:** This work was supported by the NSF grant number DMR-1609326; the Canada First Research Excellence Fund and NSERC; Fonds de Recherche du Québec-Nature et technologies; the U.S. Army Research Office grant numbers W911NF-18-1-0212, W911NF-14-1-0098, and W911NF-14-1-0103; and the Australian Research Council Centre of Excellence for Engineered Quantum Systems grant number CE170100009. S.T.F. thanks the Yale Quantum Institute for its hospitality while this research was carried out. **Author contributions:** All authors contributed to overall writing and verification of results. S.P., L.S.-J., S.M.G., S.T.F., A.B., and L.J. conceived and developed the conceptual ideas behind the CX gate, CCX gate, noise analysis, threshold calculation, and decoding. S.P., L.S.-J., S.T.F., and J.A.G. carried out numerical simulations and analytical calculations. A.G., N.E.F., and S.T. contributed to development of the experimental circuit. S.M.G. and A.B. supervised the work. P.S.I. and A.K., along with all authors contributed to overall writing and verification of results. **Competing interests:** The authors declare that they have no competing interests. **Data and materials availability:** All data needed to evaluate the conclusions in the paper are present in the paper and/or the Supplementary Materials. Additional data related to this paper may be requested from the authors.

Submitted 2 July 2019

Accepted 10 July 2020

Published 21 August 2020

10.1126/sciadv.aay5901

Citation: S. Puri, L. St-Jean, J. A. Gross, A. Grimm, N. E. Frattini, P. S. Iyer, A. Krishna, S. Touzard, L. Jiang, A. Blais, S. T. Flammia, S. M. Girvin, Bias-preserving gates with stabilized cat qubits. *Sci. Adv.* **6**, eaay5901 (2020).

Bias-preserving gates with stabilized cat qubits

Shruti Puri, Lucas St-Jean, Jonathan A. Gross, Alexander Grimm, Nicholas E. Frattini, Pavithran S. Iyer, Anirudh Krishna, Steven Touzard, Liang Jiang, Alexandre Blais, Steven T. Flammia and S. M. Girvin

Sci Adv **6** (34), eaay5901.
DOI: 10.1126/sciadv.aay5901

ARTICLE TOOLS

<http://advances.sciencemag.org/content/6/34/eaay5901>

SUPPLEMENTARY MATERIALS

<http://advances.sciencemag.org/content/suppl/2020/08/17/6.34.eaay5901.DC1>

REFERENCES

This article cites 39 articles, 2 of which you can access for free
<http://advances.sciencemag.org/content/6/34/eaay5901#BIBL>

PERMISSIONS

<http://www.sciencemag.org/help/reprints-and-permissions>

Use of this article is subject to the [Terms of Service](#)

Science Advances (ISSN 2375-2548) is published by the American Association for the Advancement of Science, 1200 New York Avenue NW, Washington, DC 20005. The title *Science Advances* is a registered trademark of AAAS.

Copyright © 2020 The Authors, some rights reserved; exclusive licensee American Association for the Advancement of Science. No claim to original U.S. Government Works. Distributed under a Creative Commons Attribution NonCommercial License 4.0 (CC BY-NC).